
Advanced Composite Materials
Publication details, including instructions for authors and subscription information:
http://www.tandfonline.com/loi/tacm20

# Interface response to solidification in sapphire-reinforced Ni-base composites

R. Asthana & S. N. Tewari

Version of record first published: 02 Apr 2012.

To cite this article: R. Asthana & S. N. Tewari (2000): Interface response to solidification in sapphire-reinforced Ni-base composites, Advanced Composite Materials, 9:4, 265-307

To link to this article: http://dx.doi.org/10.1163/15685510052000039

*Adv. Composite Mater.*, Vol. 9, No. 4, pp. 265–307 (2000)




# Interface response to solidification in sapphire-reinforced Ni-base composites

R. ASTHANA [1,*] and S. N. TEWARI [2]

[1] *Manufacturing Engineering, 326 Fryklund Hall, Technology Department, University of Wisconsin-Stout, Menomonie, WI 54751, USA*
[2] *Chemical Engineering Department, Cleveland State University, Cleveland, OH 44115, USA*

Received 2 February 1999; accepted 9 May 2000

**Abstract**—Controlled solidification of sapphire–NiAl and sapphire–Hastelloy composites was carried out to evaluate the influence of processing and alloying on the microstructure, chemistry, and interface and fiber strengths. Pressure casting, gravity casting, and zone directional solidification (DS) techniques were used to synthesize the composites. Both gravity casting and DS yielded higher interfacial shear strength in the composites compared to the solid-state powder cloth (PC) techniques. Large columnar $\beta$-NiAl grains surrounding the fibers in the DS material decreased the propensity for interfacial decohesion, resulting in a higher interface strength than in fine, equiaxed grains of gravity cast and PC composites. Alloying of NiAl matrix with Cr, W and Yb increased the interface strength relative to unalloyed NiAl but led to fiber degradation, with Yb causing the most extensive fiber damage. Pressure casting is viable to make high fiber volume fraction sapphire-reinforced Ni-base composites; however, fibers suffer strength loss (about 65 pct. relative to the virgin fiber) due to chemical attack. The residual fiber strengths are consistent with a Weibull distribution function. Controlling the strength-limiting reactions by matrix modification, use of barrier coatings, and process control (e.g. reduced temperatures) would permit exploitation of the unique potential of solidification techniques to design the composites for toughening and strengthening.

*Keywords*: Zone directional solidification; interfacial shear strength; pressure casting; nickel-base high-temperature composites; sapphire-reinforced NiAl; fiber push-out test; interfacial reactions; fiber residual strength.

## 1. INTRODUCTION

The potential of fiber-reinforced intermetallics and superalloys in advanced high-temperature applications has been explored for some time now. The aluminides of Ni, Ti, and Fe, as well as various superalloys have been reinforced with unidirectionally aligned ceramic fibers, using principally, solid-state fabrication tech-

*Corresponding author: E-mail: asthanar@uwstout.edu

niques such as powder metallurgy and diffusion bonding [1–8]. However, contamination of the fiber–matrix interface from oxides on metal powders tends to impair the strength of the interfacial bond in powder-processed composites; besides, composites that contain a binder for green strength during handling and forming often show poor interfacial shear strength because of interface contamination from binder residues. Additionally, substantial mechanical damage to the fibers could be caused during the solid-state consolidation. Liquid-phase composite fabrication techniques such as vacuum- and pressure casting [9–12], and directional solidification [13–20] have been employed to synthesize intermetallic-matrix composites such as NiAl, $Ni_3Al$, TiAl and FeAl reinforced with a variety of alumina fibers (DuPont's fibers FP and PRD166, Saphikon's single crystal sapphire, and others). Likewise, high-temperature superalloys also have been reinforced with both metals (tungsten fiber [21]) and ceramics ($Al_2O_3$ fiber [22]). However, fiber degradation at elevated temperatures by the matrix, and preform deformation and damage during fabrication present difficulties in composite manufacture using the liquid-phase techniques.

In spite of such problems, liquid-phase techniques are attractive because they offer greater flexibility in designing the matrix- and interface microstructures than solid-state consolidation techniques. For example, controlled solidification allows growth of dual-phase microstructures, single crystals, oriented crystals, and cellular and dendritic growth morphologies [23–26]. Thus, directional solidification (DS) of pseudobinary NiAl–X (X could be Mo, W, Cr Fe etc.) eutectic alloys has been used to create a matrix containing an aligned $\beta$-phase sandwiched between a ductile second phase. Likewise, DS of NiAl-rich (hypoeutectic) compositions could be used to obtain aligned cells of $\beta$-phase surrounded by the *in-situ* composite (DS eutectic) microstructure created by the solidification of the intercellular eutectic liquid. These *in-situ* composites of pseudobinary eutectic compositions significantly improve the room temperature ductility and toughness [23, 24]. While all such advantages of solidification techniques can be realized in the ceramic fiber-reinforced composites also, the issues of fiber–matrix compatibility (wettability, interface strength, and fiber degradation) must be carefully assessed.

This study focusses on the development of sapphire-reinforced nickel-base composites using the solidification and casting techniques. The emphasis is on how processing methodology and process variables influence the interface response as manifested in interfacial shear strength, interfacial decohesion, fiber residual strength, and interface microstructure and chemistry. In particular, as cast and directional solidified (DS) sapphire-reinforced $\beta$-NiAl and its ternary alloys with Cr, W and Yb, and a pressure cast sapphire-reinforced Ni-base superalloy (Hastelloy) containing reactive solutes are evaluated and compared with the solid-state (hot-pressed) composites.

## 2. EXPERIMENTAL PROCEDURE

### *2.1. Composite fabrication*

*2.1.1. Vacuum induction melting (VIM) and gravity casting.* Stoichiometric $\beta$-NiAl (equiatomic fractions of Ni and Al, Fig. 1a) and ternary alloys of NiAl with Cr and W were synthesized using induction melting under a protective, ultra-high purity (UHP) argon atmosphere, followed by casting in a high purity Cu mold. Alloying of NiAl was performed by arc-melting master alloy pellets, followed by remelting and alloying to obtain the desired chemistry. Low fiber volume fraction ($<$0.5%) composites were fabricated by laying in a copper mold sapphire fibers with fiber ends rigidly supported within holes drilled in steel caps, followed by gravity casting of molten alloy.

*2.1.2. Zone directional solidification (DS).* NiAl-matrix composites prepared using both VIM and a 'powder cloth' (PC) [2] technique were used as the feed material for DS in the floating-zone mode (Fig. 1b and c). The zone DS was carried out in a 30 kW RF induction melting unit which housed a current concentrator for efficient coupling, and a motorized traverse mechanism which permitted control of the growth speed. The DS was carried out by creating a floating molten zone (0.006$-$0.008 m long) under a 20 kPa positive pressure of UHP argon to suppress Al loss, and traversing this zone along the specimen at a controlled rate. The temperature of the floating zone was recorded by using a pair of radiation pyrometers focussed on two orthogonal surfaces of the molten zone.

*2.1.3. Pressure infiltration of composites.* Trial runs on vacuum infiltration of sapphire preforms with NiAl and Ni-base superalloy (hastelloy) were unsuccessful and led to incomplete infiltration, poor interfacial bonding, and porosity. Subsequent runs were made using a pressure infiltration technique. Three different preform fabrication procedures were used:

(a) sapphire filaments were cut to about 0.2 m length, cleaned ultrasonically in deionized water, and laid unidirectionally with their ends cemented in quartz capillaries of 300 $\mu$m internal diameter (I.D.). About 15$-$20 such fibers with capillaries attached to fiber ends were inserted in open ended, high-purity, recrystallized alumina molds (I.D. $=$ 0.006 m, length $=$ 0.20 m). Additional capillaries were cemented between the fibers near the fiber ends to permit metal suction and flow;

(b) fibers were bundled and inserted in open-ended recrystallized alumina molds to achieve tight packing; and

(c) fibers were intermixed with a small amount of NiAl powder to reduce fiber-to-fiber contact, rolled into bundles, and inserted into alumina molds prior to infiltration.

Infiltration was performed in a pressure chamber that housed a pair of induction coils, powered by a generator. Infiltration was carried out in either bottom-fill (fibers

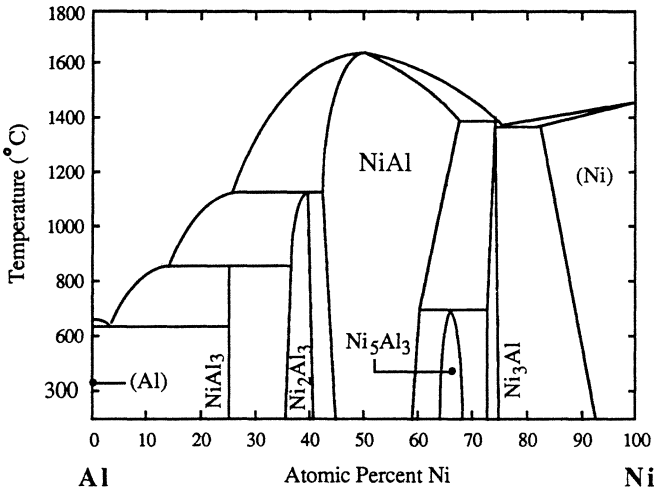


(a)

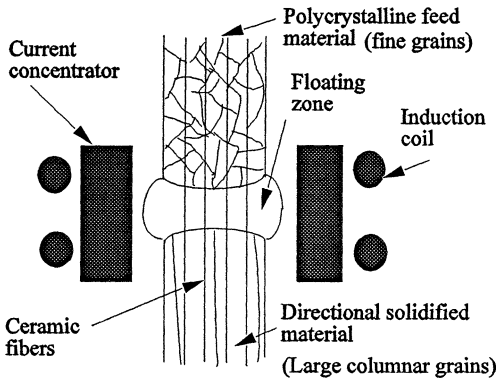


(b)

**Figure 1.** (a) Equilibrium phase diagram of Al–Ni system [26], (b) schematic of zone directional solidification of sapphire–NiAl composites, and (c) photograph showing molten zone in a test specimen during the zone DS process, and (d) schematic of pressure infiltration casting technique used for preform infiltration.

on top, melt at bottom) configuration or top-fill (melt on top, fibers at bottom) configuration. The infiltration procedure consisted of setting up the preform and the metal charge in the desired configuration (Fig. 1d), positioning the W–Re thermocouples at various locations to monitor preform- and metal temperatures, closing the pressure vessel and purging the chamber with ultra high-purity (UHP) argon gas followed by evacuation to a vacuum level of about $10^{-3}$ torr. The preform and the metal were heated simultaneously but independently using a pair of induction coils, until the desired temperatures were reached, whereupon the vessel was pressurized with UHP argon gas. At the conclusion of infiltration, the chamber was purged with argon gas to cool the samples. The solidification shrinkage during

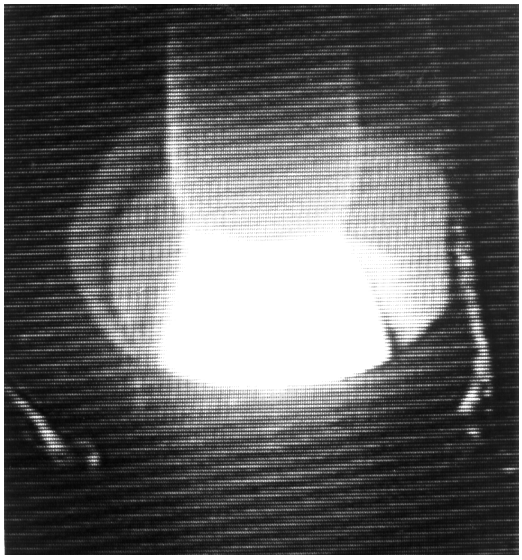

(c)

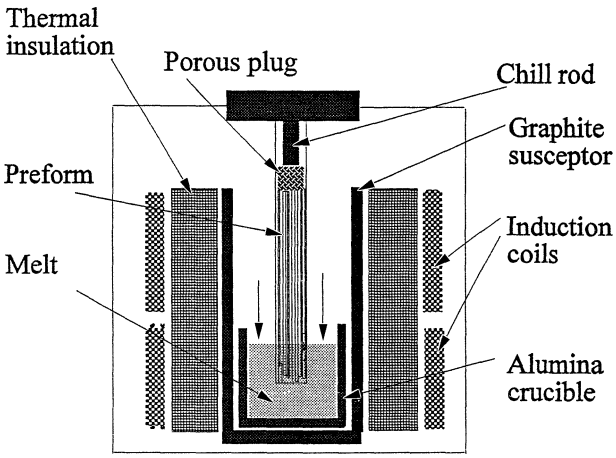


(d)

**Figure 1.** (Continued).

cooling of composite specimens was fed by use of suitably positioned chills (e.g. in the top-fill infiltration, a copper chill was placed in contact with the lower (closed) end of the alumina mold). Trial runs were also made with a graphite susceptor with tapered walls (with smaller diameter toward the melt and larger diameter toward the preform). This susceptor design was believed to allow progression of the solidification front from the bottom toward the top. Chilling was found to be more effective than use of a tapered susceptor.

### 2.2. Characterization

*2.2.1. Microstructure and chemistry.* Optical- and scanning electron microscopic examinations of composites were carried out following appropriate sample preparation procedures. The NiAl composite samples were ground, polished and etched in an aqueous solution of 25% acetic acid and 25% nitric acid. The SEM examination was carried out in a Cambridge 2000 scope with an EDS attachment. X-ray and EDS examinations of selected test specimens were done for phase identification and phase analysis. SEM fractography was used to examine the crack propagation behavior in the composites during the fiber push-out test. The chemical analysis of the test specimens was carried out using Inductively Coupled Plasma (ICP) and wet chemical analysis. The sapphire fibers were extracted from the composite matrix for microscopic examination and residual strength measurements. The fibers were extracted by dissolving the matrix in a solution of 75% acetic acid, 23% nitric acid, and 2% hydrochloric acid.

*2.2.2. Fiber strength, interface strength and microhardness.* The fiber push-out test set-up [27] records the time dependence of applied load during compresson of a fiber (embedded in a thin wafer of the matrix) using a flat bottomed punch of sintered tungsten carbide aligned over the fiber. For this purpose, flat disks or wafers of composite specimens were first cut, ground and polished to metallographic surface finish. To examine the effect of disk thickness on the fiber push-out behavior, disk thicknesses in the range 230 to 720 $\mu$m were used. The polished disks were then firmly glued to a steel sample holder having 400 $\mu$m wide grooves, taking care to align the fibers over the grooves so as to enable their unobstructed sliding during the fiber push-out. A motorized traverse mechanism allowed the sample to be moved toward the stationary punch at a rate of 0.82 $\mu\mathrm{m\,s}^{-1}$. The load versus time data were recorded at 50 milliseconds intervals for a period of 3 minutes or less, and stored in computer files. The acoustic emission response generated during the fiber push-out was also recorded. Typically, ten to thirty fibers were tested for a given set of processing conditions, and the load–time data were transformed into stress–displacement plots as explained in Section 3.2.1. The stress–displacement profile for each fiber was examined with reference to the decohesion behavior as revealed in the SEM views of the fracture surface. Several samples were tested using the interrupted fiber push-out test in conjunction with SEM fractography to identify the onset of deformation of the disk, and crack initiation and growth behaviors. For this purpose, all the fibers in a given wafer were 'tagged' on low-magnification photomicrographs for identification, and were examined under the SEM after stopping the push-out test at two or three different load transitions during the push-out. The thermal fatigue resistance of as-fabricated composites was characterized by measuring the interfacial shear strength of the test samples after thermal cycling in air (500 cycles, 400 K (15 min soak) to 1273 K (10 min soak)). Additionally, the fiber srength measurements were made on extracted fibers using an instron frame. A gauge length of $1.27 \times 10^{-2}$ m, a grip distance of 0.114 m and

a cross-head speed of $1.27 \times 10^{-3}$ m min$^{-1}$ were used. The microhardness profiles near the fiber–matrix interface were measured using a Buehler microhardness tester with a knoop indentor and 0.30 kg load.

## 3. RESULTS AND DISCUSSION

### *3.1. Chemistry and microstructure*

*3.1.1. Powder cloth (PC) and gravity cast sapphire–NiAl.* The microstructures of both 'powder cloth' (PC) (Fig. 2a) and gravity-cast specimens consisted of a fine NiAl grain structure, and some interfacial- and matrix porosity due either to incomplete sintering (in the PC specimens), or inadequate wetting between the fiber and the NiAl matrix (in the gravity cast specimens). In gravity-cast sapphire–NiAl(Cr) and sapphire–NiAl(W) specimens, however, interfacial bonding was better. As the fiber volume fraction was low (<0.5%) in the gravity-cast test composites, metal penetration of interfibers spaces did not present a major problem.

*3.1.2. Zone directional solidification (DS).*

*3.1.2.1. DS optimization.* Both as-cast (AC) and powder-cloth (PC) feedstocks were used for 'floating zone' directional solidification (DS). Melt temperature was a critical parameter for zone stability and fiber integrity during the DS; a temperature of 2033 K led to fiber breakage and specimen deformation, whereas a temperature of 1993 K was near optimum, and did not lead to appreciable change in the shape of the composite feedstock specimen (Fig. 2b). During floating zone DS with the help of an induction heater, an axisymmetric electromagnetic field pushes the melt zone toward the center of the flux concentrator, and extensive convection is caused by the eddy currents. While the fibers dampen fluid convection and reduce the tendency for the sample shape distortion, vigorous convection caused by a departure from the optimum zone temperature increases the tendency for fiber fragmentation and zone instability.

*3.1.2.2. Sapphire–NiAl.* The directional solidification (DS) of powder cloth (PC) and as cast (AC) feedstocks led to large columnar grains (Fig. 2g) aligned along the growth direction; the average matrix grain sizes in the PC and DS specimens were approximately 50 $\mu$m and 1000 $\mu$m, respectively. In the DS specimens, grain boundaries appear to migrate past the fibers (Fig. 2d), leading to fibers that are either anchored to a few (two-to-three) grain boundaries, or are completely engulfed within the grain interior (Fig. 2c–f). The fibers anchored at grain boundaries in the DS specimens are termed *GB fibers*, whereas the fibers that are embedded within the grain interior are termed *GI fibers*. The progressive elimination of grain boundaries from the fiber vicinity suggests that the zone DS technique could potentially allow growth of single crystal NiAl-matrix composites reinforced with ceramic fibers for both toughening (from single crystalline matrix) and strengthening (from fibers).

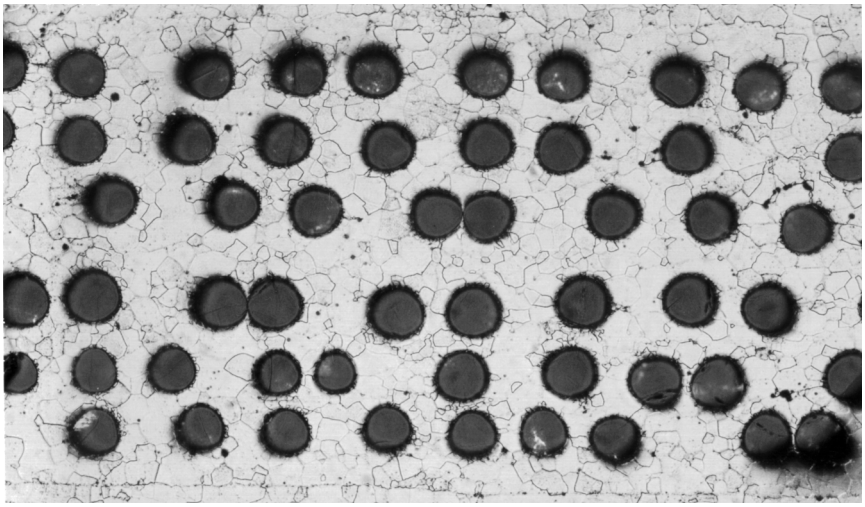

(a)

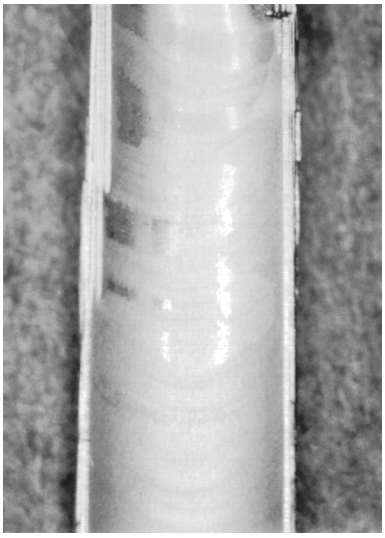

(b)

**Figure 2.** Photomicrographs showing (a) powder-cloth (PC) sapphire–NiAl composite used as a feedstock for zone DS, (b) directional solidified (DS) sapphire–NiAl composite bar, (c) and (d) DS microstructure showing fibers engulfed within the $\beta$-NiAl grains (GI fibers), and fibers anchored at grain boundaries (GB fibers) in the DS specimens made from (c) PC feedstock, and (d) gravity-cast low fiber volume fraction (<0.5%) feedstock, (e) and (f) $\beta$-NiAl grain structure in the vicinity of a sapphire fiber in the (e) PC, and in the (f) DS specimens, and (g) columnar $\beta$-NiAl grains in a DS specimen.

The melt convection in the floating zone leads to some fiber breakage in the DS specimens just as the hot consolidation of solid-state powder-cloth (PC) composites results in fiber damage (Fig. 3).

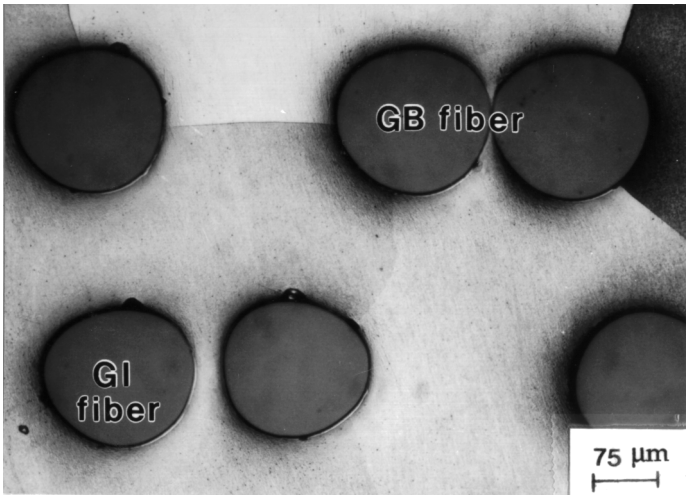


(c)

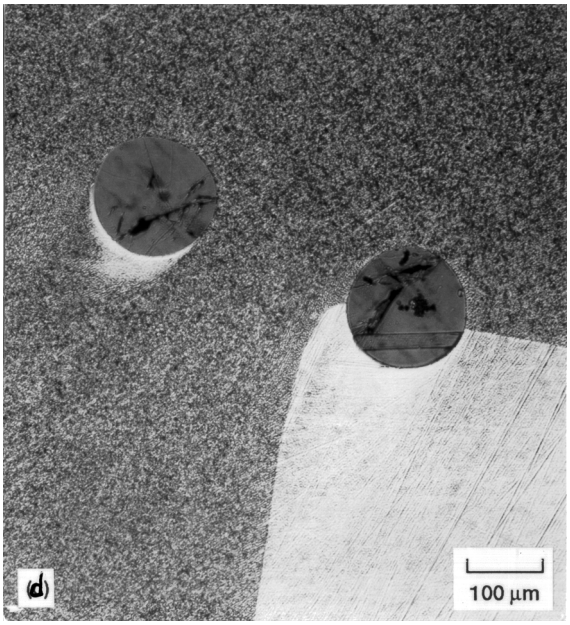


(d)

**Figure 2.** (Continued).

*3.1.2.3. Sapphire–NiAl(Cr).* The composition (in wt%) of NiAl(Cr) matrix to 5% relative accuracy is 28.2Al–11.4Cr–60.2Ni; the average oxygen concentration is about 300 ppm. The NiAl(Cr) phase diagram (Fig. 4a) suggests formation of NiAl–Cr eutectic which is seen in the cellular microstructure of the DS test specimens, with the eutectic residing in the intercellular regions. Chromium preferentially precipitates onto the fibers (Fig. 4b) and appears well bonded to the

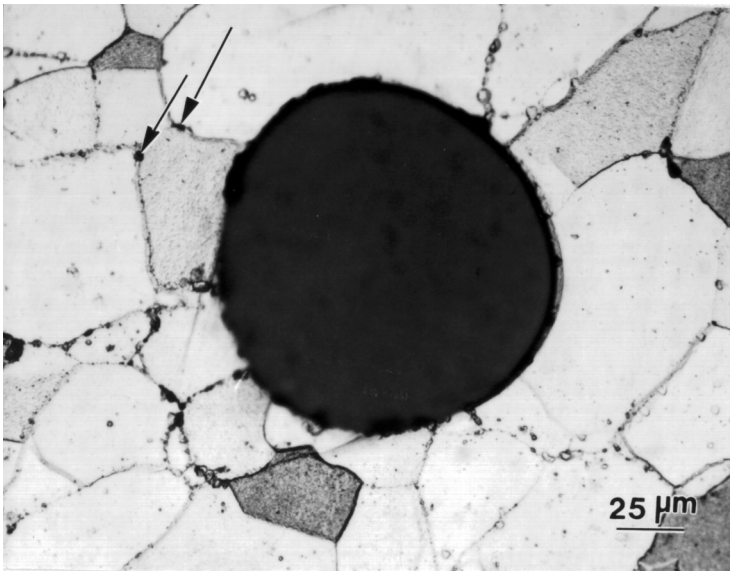


(e)

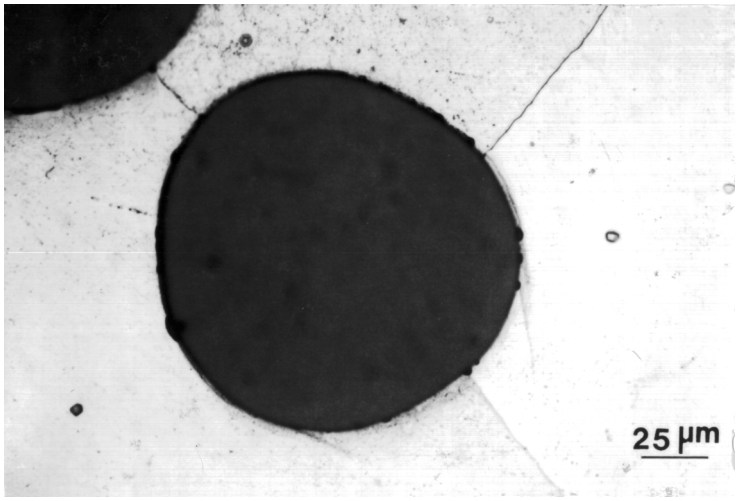


(f)

**Figure 2.** (Continued).

fiber (Fig. 4c). The chromium precipitates present within the NiAl cells form by the solid-state precipitation from the supersaturated NiAl matrix upon cooling.

The extracted fibers show evidence of chemical attack in the form of pits (Fig. 4d) which would serve as local stress raisers and sites for premature fiber failure. The critical size, $c$, at which a surface flaw extends into a damaged fiber is related to the fiber tensile strength, $\sigma_f$, by [4, 28], $\sigma_f = 0.893[E_f G_c/\pi c]^{0.5}$ where $E_f$ is the fiber modulus, and $G_c (= K_{Ic}^2/E_f)$ is the strain energy release rate of fiber. For single

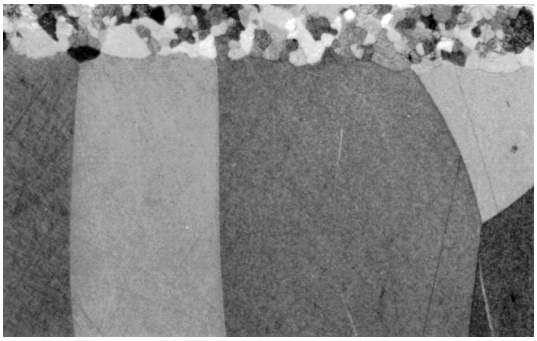

(g)

**Figure 2.** (Continued).



crystal alumina, $K_{Ic} \approx 2.38$ MPa m$^{0.5}$ [4], $E_f = 435$ GPa, $\sigma_f = 2.7$ GPa [29], so that the critical flaw size $c$ is obtained as 0.2 $\mu$m. As the critical flaw size is quite small, the surface pits on the sapphire from chemical attack (Fig. 4d) could become strength-limiting. It is noteworthy that, in the solid-state processed NiAl- and superalloy composites also, the strength of sapphire degrades by almost 50% or more [4, 5, 8].

*3.1.2.4. Sapphire–NiAl(W).* The composition of the NiAl(W) matrix is: 31.4Al–1.5W–67.4Ni and 300 ppm oxygen. Large columnar NiAl grains characterize the structure of the DS material; however, unlike the chromium precipitates in the directional solidified (DS) NiAl(Cr), the tungsten-rich particles do not preferentially precipitate onto the fiber surface (Fig. 4e), suggesting a relative lack of chemical affinity of tungsten toward $Al_2O_3$. The fiber–matrix interfaces are clean, and no gross fiber damage appears to have occurred.

*3.1.2.5. Sapphire–NiAl(Yb).* The average grain sizes of the powder cloth (PC) and directional solidified (DS) NiAl(Yb) specimens were 80 $\mu$m and 230 $\mu$m, respectively. The chemical and X-ray phase analyses of composite specimens are given in Table 1. Extensive chemical attack of fibers by the matrix appears to have taken place in both the PC and DS specimens (Fig. 5c and d) in contrast to the fibers in the DS NiAl–sapphire specimens without Yb (Fig. 5a and b), where no evidence of chemical attack was noticed at comparable magnifications. The extent of attack in the NiAl(Yb) composites increased after directional solidification (DS), and led to a multiphase interlayer together with excessive fiber surface reconstruction. The Al, O, and Yb images on fibers extracted from the NiAl(Yb) matrix are shown in Fig. 5e–h. The oxide of Yb ($Yb_2O_3$) is stabler than $Al_2O_3$, and a reaction between the sapphire and ytterbium is expected from the thermodynamic considerations (the free energies of formation of $Yb_2O_3$ and $Al_2O_3$ are $-1727.5$ kJ mol$^{-1}$ and $-1583.1$ kJ mol$^{-1}$, respectively). The reaction products identified using the phase analysis were $Yb_2O_3$ and $Yb_3Al_5O_{12}$ [14, 16]. Figure 6 shows the various interfacial reaction product phases that formed in the PC and DS NiAl(Yb) specimens. The Ni and Al

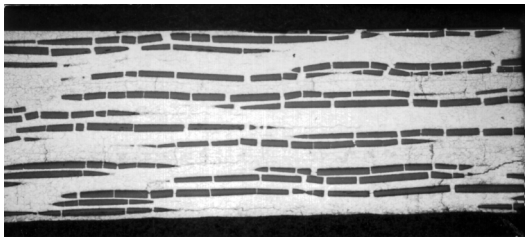

(a)

(b)

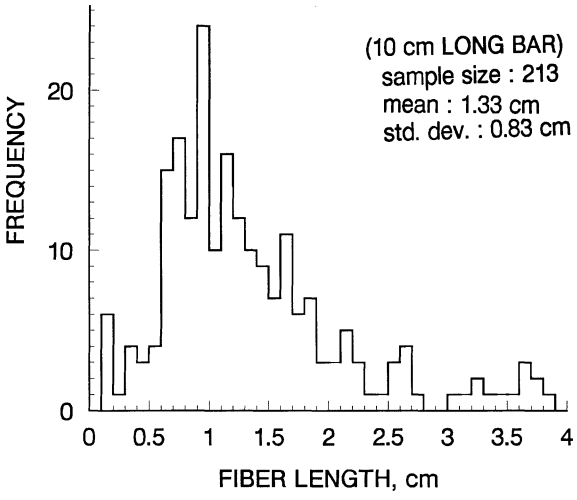


(c)

**Figure 3.** Fiber breakage during composite fabrication in the PC and in the DS processes: (a) powder-cloth specimens, (b) zone DS specimen, and (c) frequency histogram for fiber length distribution in the DS specimen.

contents of the NiAl(Yb) matrix did not change during processing, but a near 50% reduction in the amount of Yb occurred after DS (Table 1) [14, 16].

*3.1.3. Pressure infiltration of sapphire-hastealloy composites.*

*3.1.3.1. Process optimization.* The counter-gravitational (bottom-fill) infiltration generally led to unsound castings even at pressures as high as 3.5 MPa with evidence

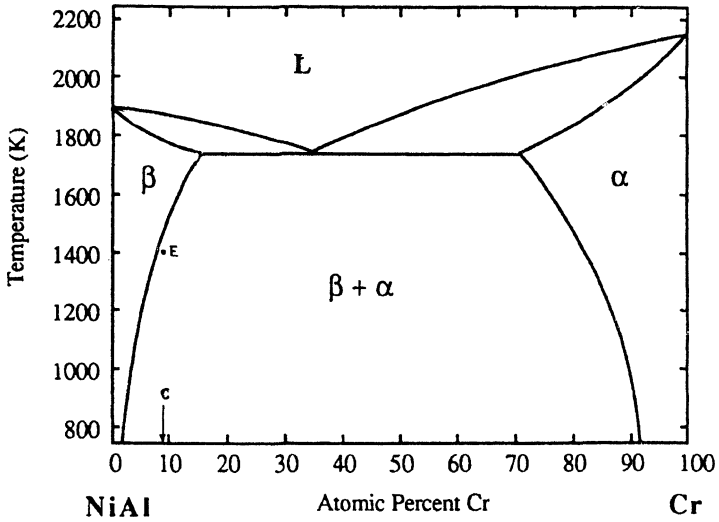


(a)

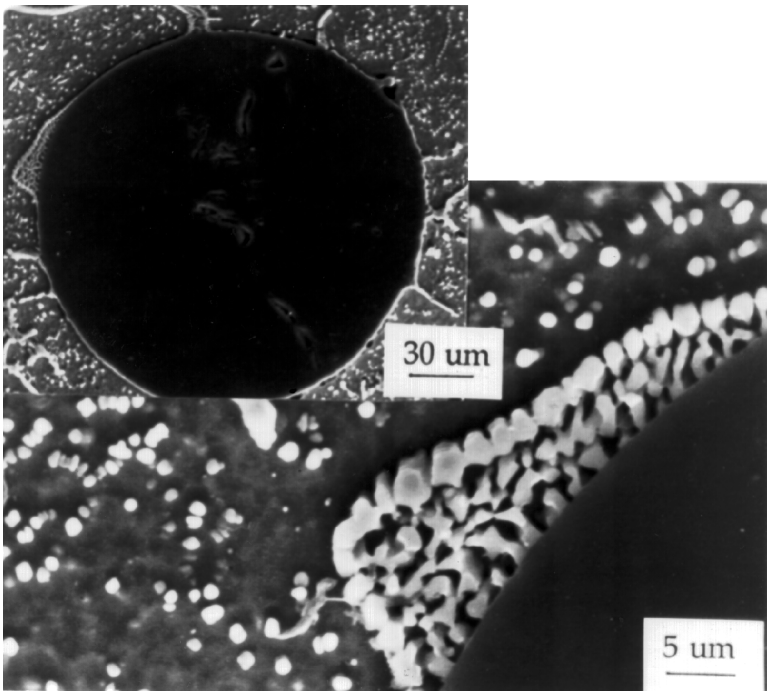


(b)

**Figure 4.** (a) Pseudobinary NiAl–Cr phase diagram [26], (b) DS microstructure of a sapphire–NiAl(Cr) specimen showing interfacial segregation of Cr onto the fibers, (c) cellular microstructure of DS sapphire–NiAl(Cr) specimens showing intercellular eutectic, and good interfacial bonding between Cr precipitates and sapphire fiber, (d) fiber pitting and adhesion of Cr precipitates to the fiber on the surface of an extracted sapphire fiber, and (e) microstructure of a DS sapphire–NiAl(W) specimen made from gravity cast feedstock (fiber vol. fr. $< 0.5\%$).

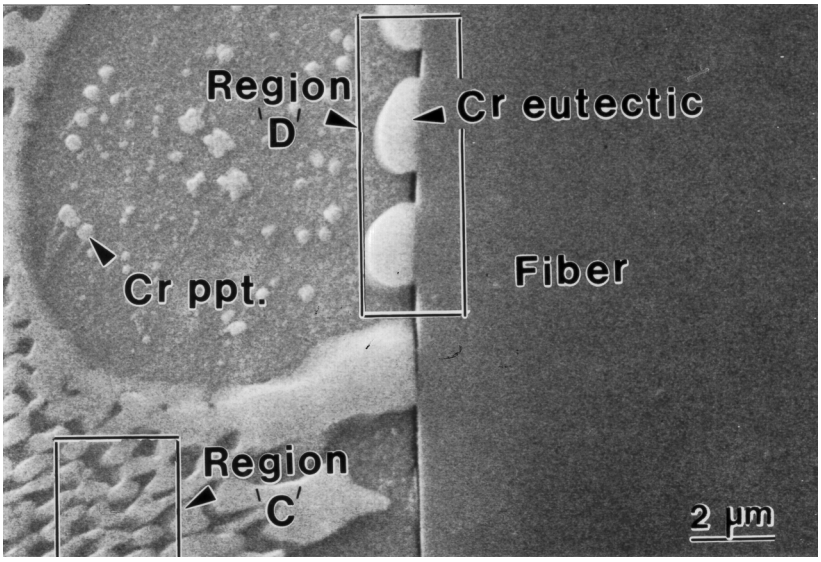


(c)

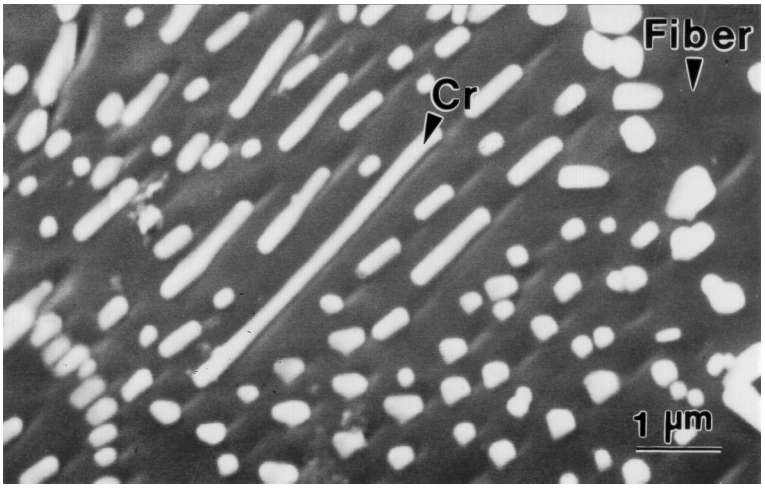


(d)

**Figure 4.** (Continued).

of fiber clumping, deformed casting, and incomplete infiltration. On the other hand, the top-fill infiltration yielded sound castings with good metal penetration of interfiber spaces even at lower infiltration pressures. The amount of metal in the crucible had to be carefully controlled; both inadequate and excess metal resulted in incomplete infiltration. In one bottom-fill infiltration run, the charge melted, overflowed the side of the alumina crucible and filled the annulus between the susceptor and the crucible; as a result, the alumina crucible floated up and blocked the passage of the metal into the preform (which resided in an alumina tube) when

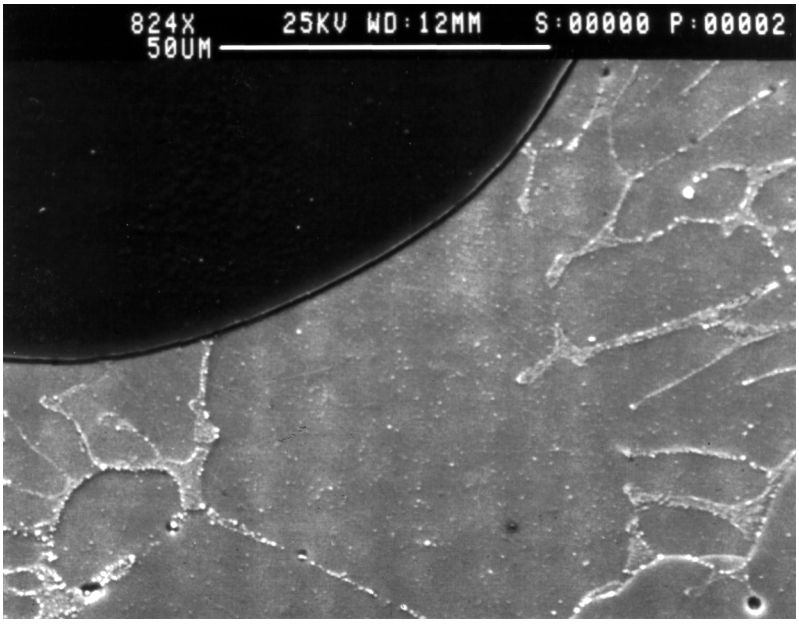


(e)

**Figure 4.** (Continued).

**Table 1.**
Chemical composition and phase analysis of sapphire–NiAl composites

| Material | Ni (atom %) | Al (atom %) | Yb (atom %) | Phases present |
|---|---|---|---|---|
| PC NiAl | 49.9 | 50.1 | — | NiAl and $Al_2O_3$ |
| DS NiAl | 50.3 | 49.7 | — | NiAl and $Al_2O_3$ |
| PC NiAl(Yb) | 62.1 | 36.8 | 0.36 | NiAl, $Al_2O_3$, $Yb_2O_3$, and $Yb_3Al_5O_{12}$ |
| DS NiAl(Yb) | 62.5 | 36.4 | 0.19 | NiAl, $Al_2O_3$, $Yb_3Al_5O_{12}$, $Ni_3Al$ |

pressure was applied to initiate the infiltration. In this case, no metal penetrated the fiber bundle. With bottom-fill infiltration, fast pressurization usually led to mold cracking and loss of pressure differential; only slow or stepped infiltration (in steps of about 80 kPa per second) prevented mold cracking. In the top-fill configuration, infiltration was less sensitive to the rate of pressurization; slow, fast and stepped (interrupted) pressurization all yielded good infiltration. Rapid pressurization also tends to chill the metal surface thereby making infiltration more difficult to accomplish. Post-infiltration cooling was a critical factor; a rapid surge of Ar led to mold cracking, loss of liquid from partially solid casting, and/or stress cracks in the casting, whereas slow cooling achieved by a controlled decrease of power to about 800°C, followed by a cold blast of Ar eliminated such defects.

*3.1.3.2. Microstructure and chemistry.* The matrix alloy composition in the sapphire–hastealloy specimens was (in wt%) 47.5Ni, 21.5Cr, 17.8Fe, 8.3Mo,

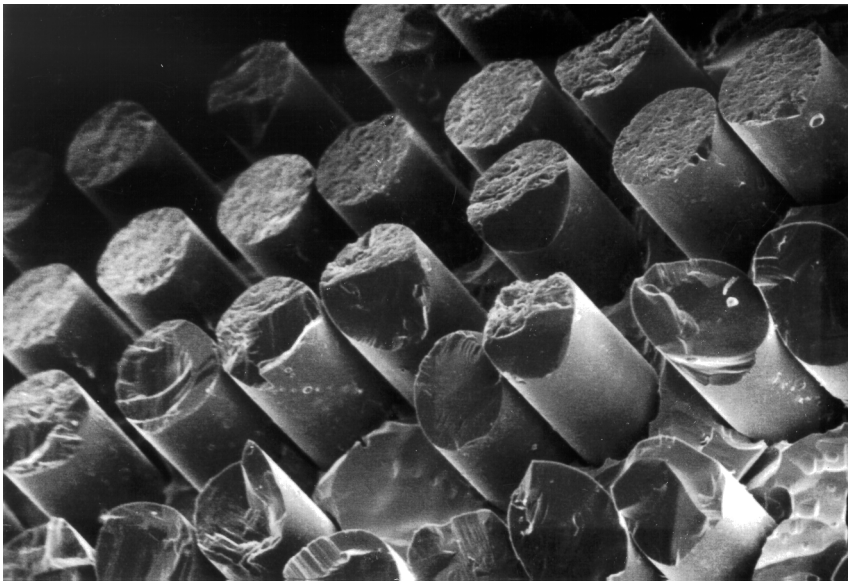

(a)

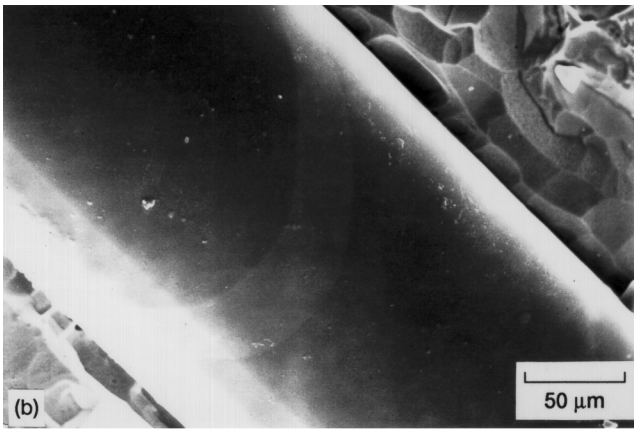


(b)

**Figure 5.** Photomicrographs showing sapphire fibers extracted from (a) and (b) zone DS sapphire–NiAl, (c) powder-cloth (PC) sapphire–NiAl(Yb), and (d) and (e) DS sapphire–NiAl(Yb) showing complex multiphase surface structure; (f) through (h) show (f) O image, (g) Al image, and (h) Yb image of the zone DS fiber of Fig. 5d.

1.7Co, 0.3Mn, 0.4Si, 0.2Al, 0.1Cu, 0.4Nb, 0.06Ti, 0.08C and 0.02 oxygen. Figure 7 shows fiber distribution and the fiber–matrix interface in a typical sapphire–hastelloy composite specimen synthesized using the pressure infiltration casting technique. The SEM examination of specimens showed that fiber distribution influenced the extent of chemical attack; regions with a high fiber packing density (small fiber spacing) exhibited little fiber damage whereas regions where

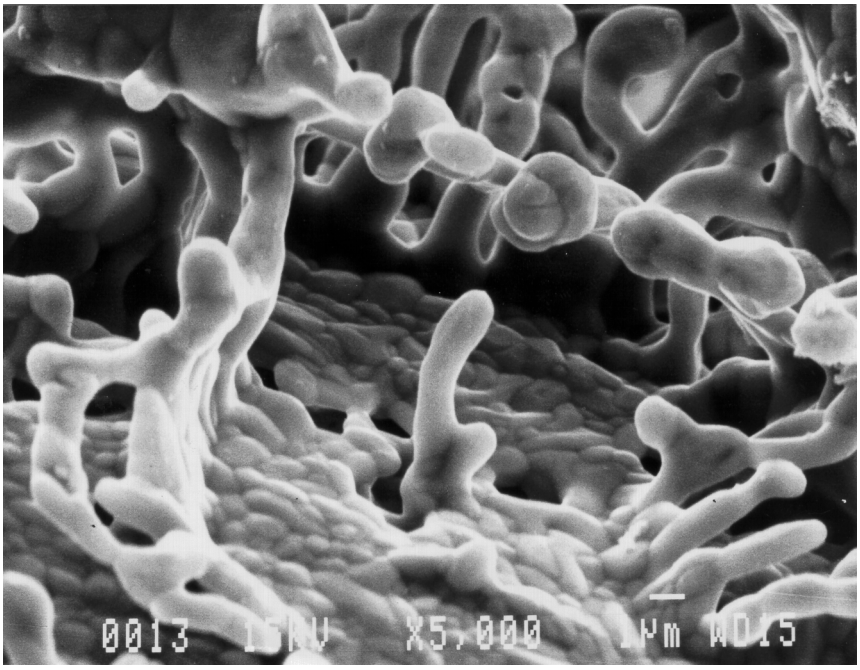


(c)

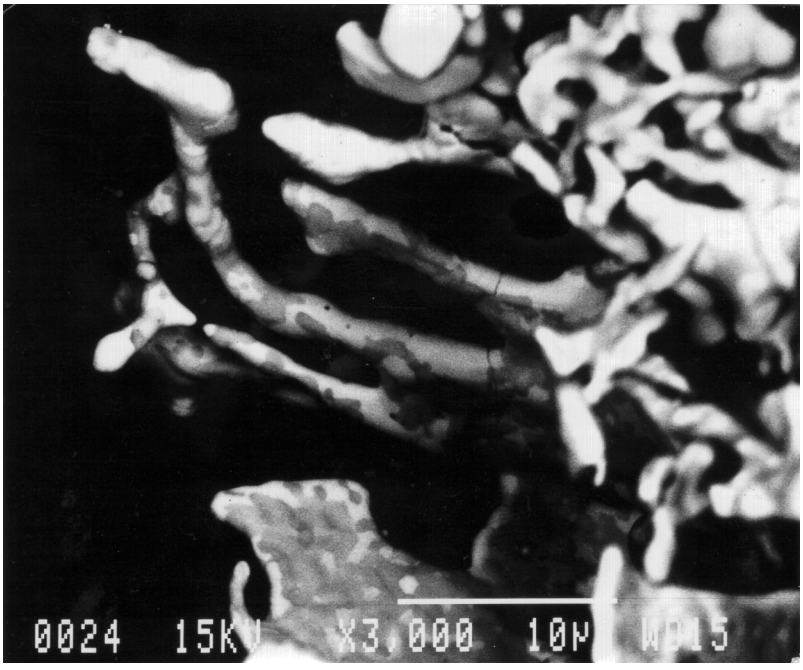


(d)

**Figure 5.** (Continued).

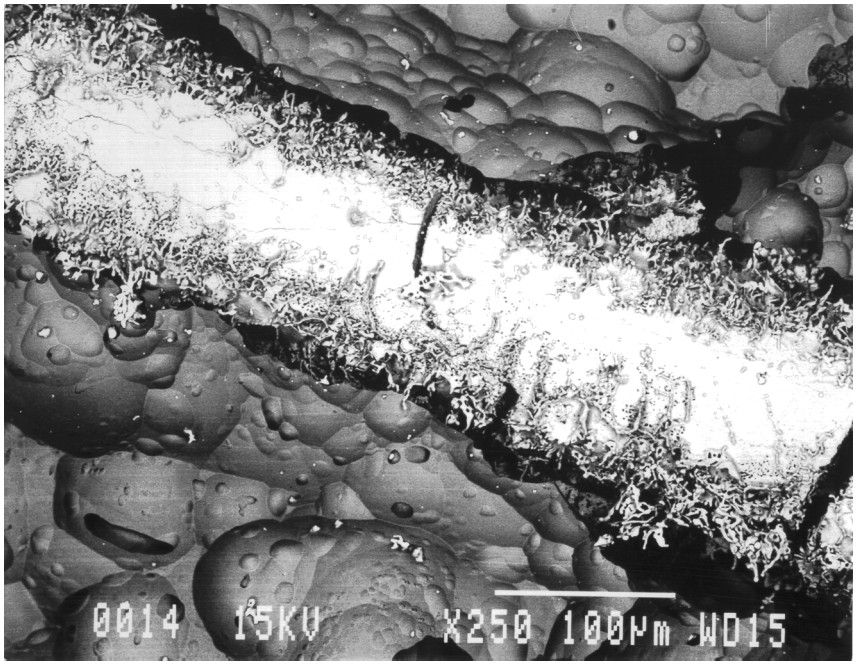


(e)

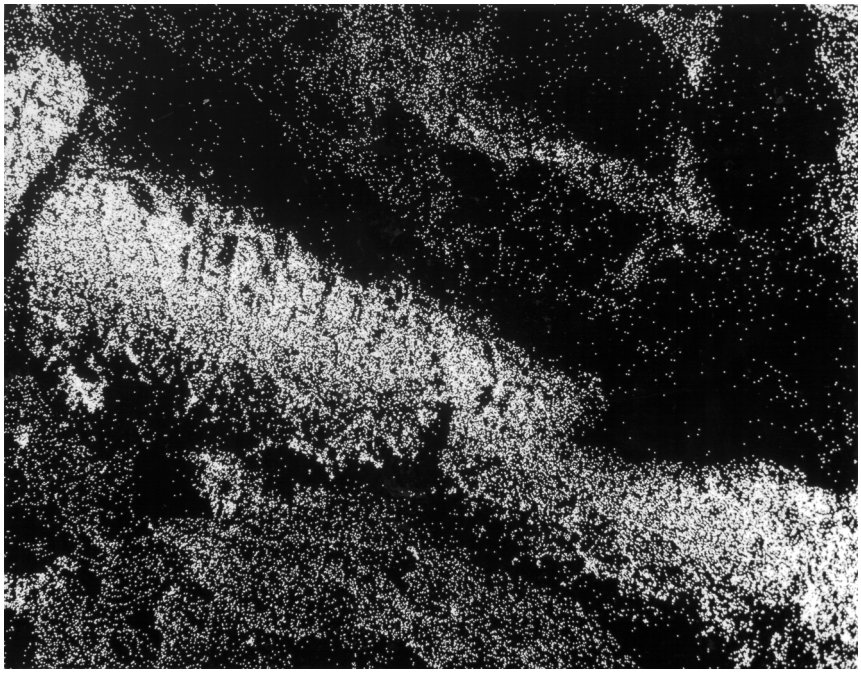

(f)

**Figure 5.** (Continued).

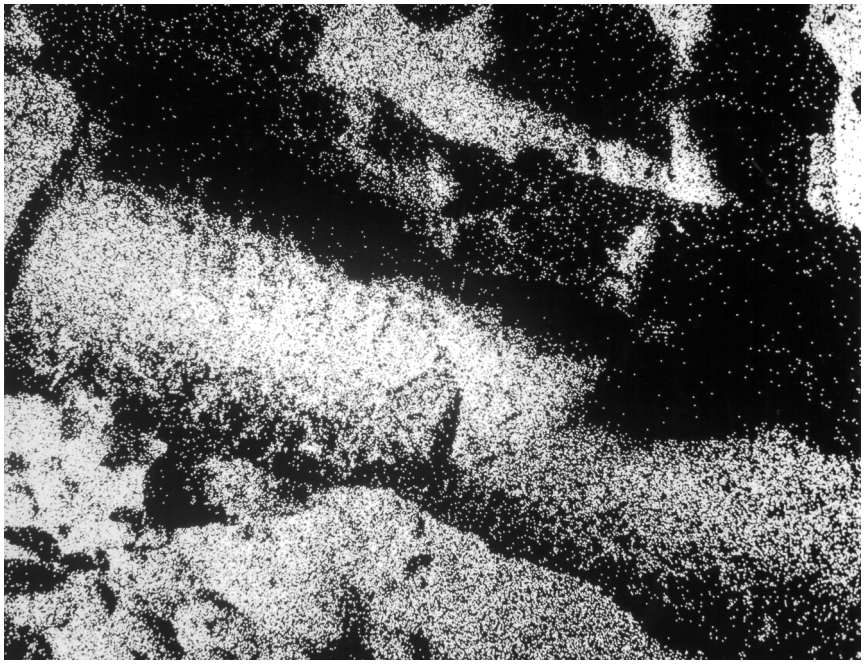

(g)

(h)

**Figure 5.** (Continued).

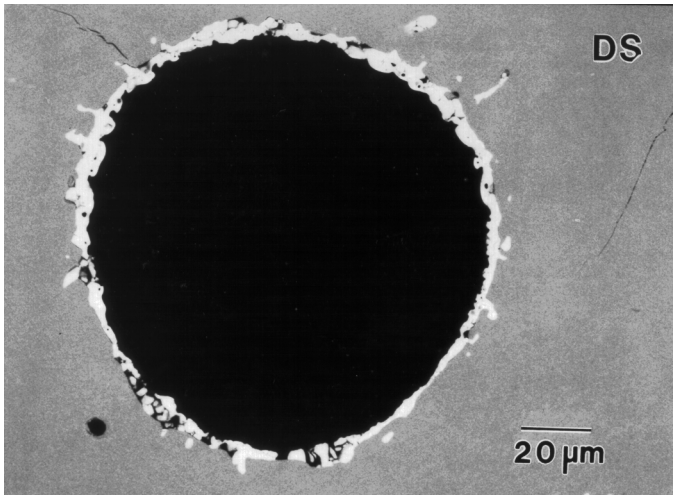


(a)

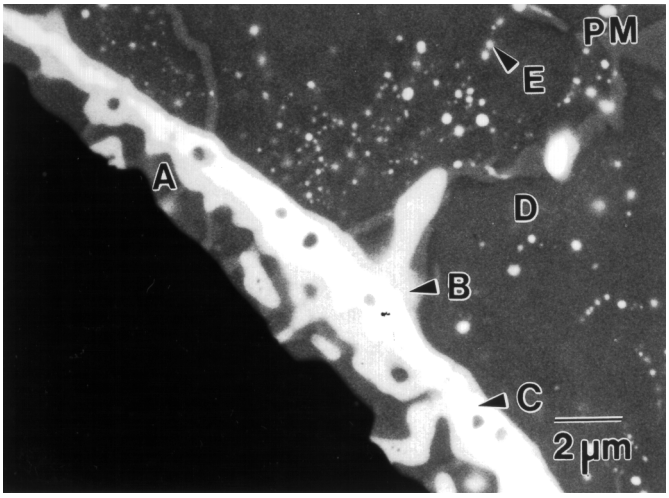


(b)

**Figure 6.** (a) Interfacial reaction zone in a DS sapphire–NiAl(Yb) composite, and (b) and (c) SEM views of the interfacial zone in (b) powder-cloth (PC) specimen and (c) zone DS specimen showing different phases at the interface (A: O-rich NiAl, B: $Yb_3Al_5O_{12}$, C: $Yb_2O_3$, D: NiAl). The fluoride compound (YbF) marked in the figure formed due to reaction with fluoride-based binders used in the powder-cloth feedstock specimen.

a relatively large pool of metal was in contact with the fibers (large fiber spacing), significant fiber damage due to interfacial reactions was observed. In other words, extensive fiber damage occurred in fiber-impoverished regions where fibers were surrounded by a relatively large area of the matrix whereas less fiber damage occurred in fiber-rich areas. This difference is presumably due to the smaller amounts of reactive solutes in fine pores between tightly packed fibers and a rela-

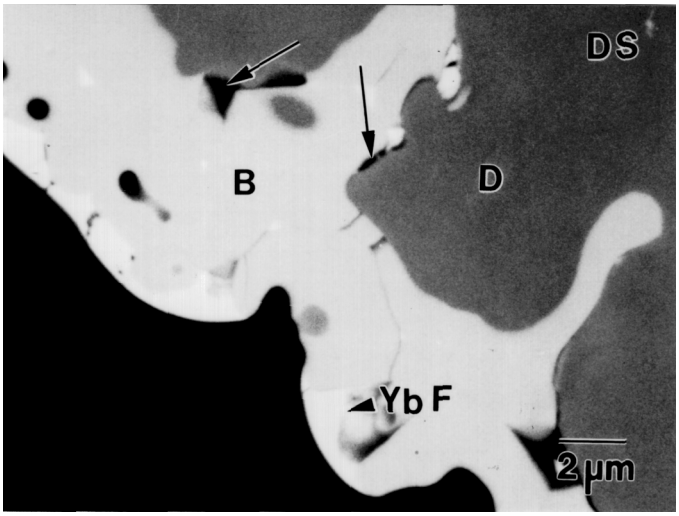


(c)

**Figure 6.** (Continued).



tively smaller sink for the diffusion of solutes released by reactions in such pores. The fiber damage was believed to be caused due to a chemical reaction between sapphire and the reactive solutes in the matrix such as chromium (also observed in sapphire–NiAl(Cr) composites [12, 13]). The extracted fibers were very brittle and difficult to handle, and in fact, only a relatively small number could be recovered for residual strength testing.

### *3.2. Interface strength and decohesion behavior*

*3.2.1. Sapphire–NiAl composites.* The fiber push-out test has been used to measure interface strength in a variety of fiber-reinforced materials such as SiC/Ti, glass/TiAl, sapphire/Nb, sapphire/NiAl and $SiC/Si_3N_4$ composites [30–45]. In this test, a fiber embedded within a matrix is loaded in compression using a microindentor, and the load required for interfacial debonding and sliding is measured as a function of the displacement. The interfacial shear stress, $\tau$, is then calculated from the relationship $\tau = load/\pi Dt$, where $D$ is fiber diameter (130 $\mu$m), and $t$ is the disk thickness. In the present study, the stresses corresponding to the three load transitions shown in Fig. 8a were considered important to characterizing the fiber–matrix interface strength. These stresses are: $\tau_p$ (proportional shear stress), $\tau_m$ (maximum shear stress), and $\tau_f$ (frictional shear stress). Table 2 and Figs 8 and 9 present interfacial shear strength data and microstructure of debonded interfaces from the fiber push out tests performed on the as cast (AC), powder-cloth (PC) and directional solidified (DS) composites used in this study.

Figure 8b and c show debonded interfaces in the directional solidified (DS) specimens in the region of displaced fibers that were originally anchored at grain

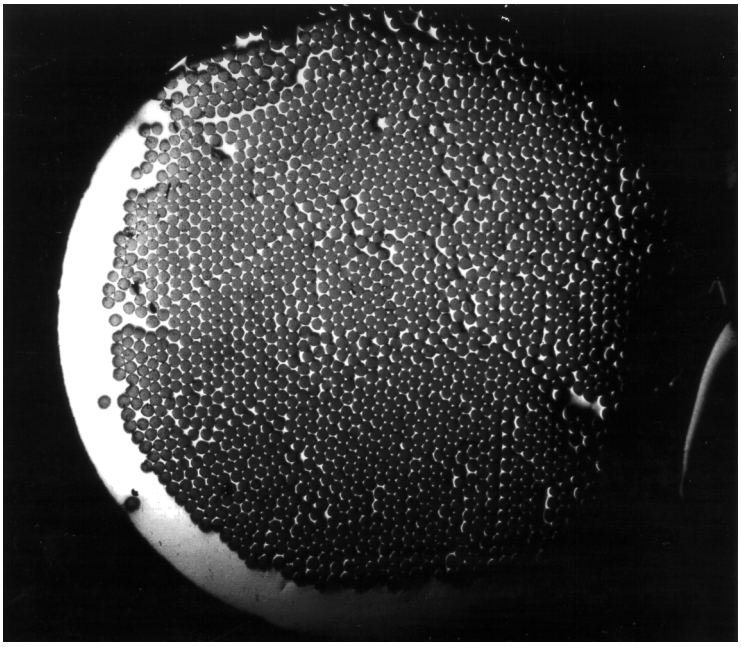

(a)

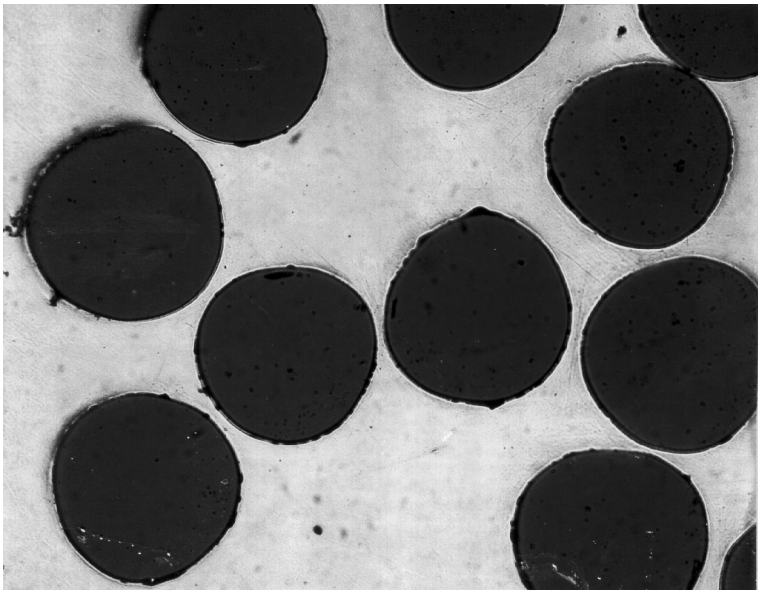

(b)

**Figure 7.** Transverse views of a pressure cast sapphire–hastelloy composite specimen showing fiber distribution in the matrix: (a) low magnification view and (b) higher magnification view showing the interface.

**Table 2.**
Mean and standard deviation of interfacial shear strengths ($\tau_p$, $\tau_m$ and $\tau_f$) in sapphire–NiAl composites

| Composite | $\tau_p$ (MPa) | $\tau_m$ (MPa) | $\tau_f$ (MPa) |
|---|---|---|---|
| Powder cloth sapphire–NiAl [PC] | 30 ± 14 | 42 ± 21 | 22 ± 9 |
| Directional solidified powder cloth NiAl feedstock [PC + DS] | 84 ± 40 | >138 ± 62 | 27 ± 7 |
| PC + DS sapphire–NiAl (data for fibers at grain boundaries) [DS(GB) fibers] | 82 ± 32 | >89 ± 40 (33) | 28 ± 15 |
| PC + DS sapphire–NiAl (data for fibers engulfed within grains) [DS(GI) fibers] | 97 ± 39 | >123 ± 32 (4) | 32 ± 11 |
| Powder cloth sapphire–NiAl(Yb) [PC] | 177 ± 64 | >205 ± 69 (24) | 126 ± 16 |
| Directional solidified powder cloth NiAl(Yb) feedstock [PC + DS] | 47 ± 28 | 67 ± 44 | 53 ± 41 |
| As cast (gravity cast) sapphire–NiAl [AC] | 91 ± 60 | 133 ± 79 | 48 ± 40 |
| Directional solidified gravity cast sapphire–NiAl feedstock [AC + DS] | 78 ± 32 | >182 (4) | 10 |
| Directional solidified and thermal cycled NiAl specimen [DS + TC] | 142 ± 37 | >170 ± 17 (3) | 75 |
| As cast (gravity cast) sapphire–NiAl(Cr) [AC] | 114 ± 36 | 154 ± 55 | 72 ± 39 |
| Directional solidified gravity cast sapphire–NiAl(Cr) feedstock [AC + DS] | 127 ± 47 | >155 ± 41 (1) | 72 ± 35 |
| As cast and thermal cycled sapphire–NiAl(Cr) [AC + TC] | 93 ± 39 | >104 ± 38 (2) | 43 ± 27 |
| Directional solidified and thermal cycled sapphire–NiAl(Cr) [DS + TC] | 146 ± 40 | >174 ± 40 (5) | 91 ± 41 |
| As cast (gravity cast) sapphire–NiAl(W) [AC] | 158 ± 71 | >168 ± 71 (3) | 41 ± 24 |
| Directional solidified gravity cast sapphire–NiAl(W) feedstock [AC + DS] | 100 ± 41 | >159 ± 69 (1) | 28 ± 13 |

[1] The proportional shear stress $\tau_p$, the maximum shear stress $\tau_m$, and the frictional shear stress $\tau_f$ are defined in Fig. 8a.

[2] The sign '>' in the $\tau_m$ values indicates that interfacial debond stress, $\tau_m$, is greater than the value shown. This is because the loading capacity of the instrument was reached without the fiber being pushed out. The number of fibers that could not be pushed is shown in parentheses after $\tau_m$ values.

[3] Interfacial shear strength data are averages for fiber push-out test specimens of thickness in the range 230 to 720 $\mu$m.

[4] PC: powder cloth; AC: as-cast (gravity cast); DS: directional solidified; PC + DS: directional solidified powder cloth feedstock; TC: thermal cycled; DS(GB) fibers: fibers anchored to grain boundaries in the DS test specimen; DS(GI) fibers: fibers completely engulfed within the NiAl grains in the DS test specimen.

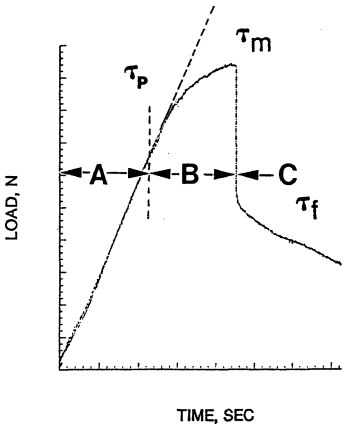


(a)


(b)

**Figure 8.** (a) Schematic load–time profile in a fiber push-out test showing pseudoelastic deformation region (A), the inelastic region (B), and frictional region (C). Also shown are the stress transitions in the load–time profile: $\tau_p$ = proportional shear stress, $\tau_m$ = maximum shear stress, $\tau_f$ = frictional shear stress, (b) front-face view of the debonded interface at a GB-fiber in a DS sapphire–NiAl specimen (note the interfacial porosity from the binder residues of PC feedstock, and interfacial cracking at the grain boundary during push out), (c) front-face view of the debonded interface at a GI-fiber in a DS sapphire–NiAl, and (d) pseudoelastic deformation of test wafers at 1.37 N load in the regions of PC-, GB- and GI-fibers at various wafer thicknesses (1.37 N is the smallest load corresponding to $\tau_p$ in the experiments).

boundaries (GB fiber) and the fibers that resided within the NiAl grains (GI fiber). Figure 9e–g show histograms for the interfacial shear strengths $\tau_p$, $\tau_m$, and $\tau_f$ for fibers in the DS and PC test specimens at various values of the disk thickness-to-support span ratio ($t/h$), where $t$ is the thickness of the disk and $h$ is the support span width ($\sim$400 $\mu$m) on the specimen holder that was used in the fiber push-out

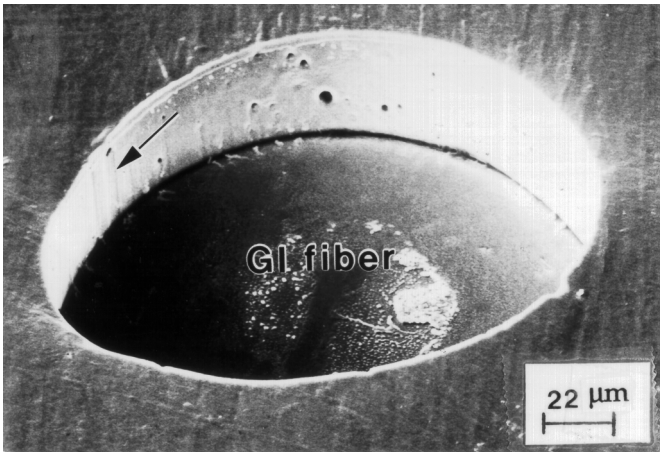


(c)

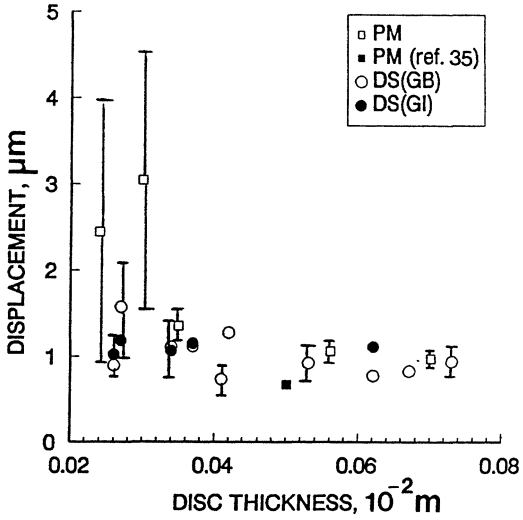


(d)

**Figure 8.** (Continued).

test. The proportional shear stress ($\tau_p$) which signals the onset of debond initiation is greater for the DS composites (84 $\pm$ 40 MPa) than the PC composites (30 $\pm$ 14 MPa). Also significant is the difference in the proportional shear stress values for the fibers residing within the NiAl grains (GI fibers) and those anchored at a few grain boundaries in the DS material (GB fibers). The mean $\tau_p$ (97 $\pm$ 39 MPa) of the GI fibers is greater than the $\tau_p$ (82 $\pm$ 32 MPa) of both the GB fibers and the fibers in the powder cloth (PC) specimens (30 $\pm$ 14 MPa). The interfacial bond is, therefore, strongest for the fibers located within the NiAl grains of the DS specimens (GI fibers) and weakest for the fibers in the powder-cloth (PC) specimens. The large number of grain boundaries coincident on the fibers in the PC specimens lead to easy

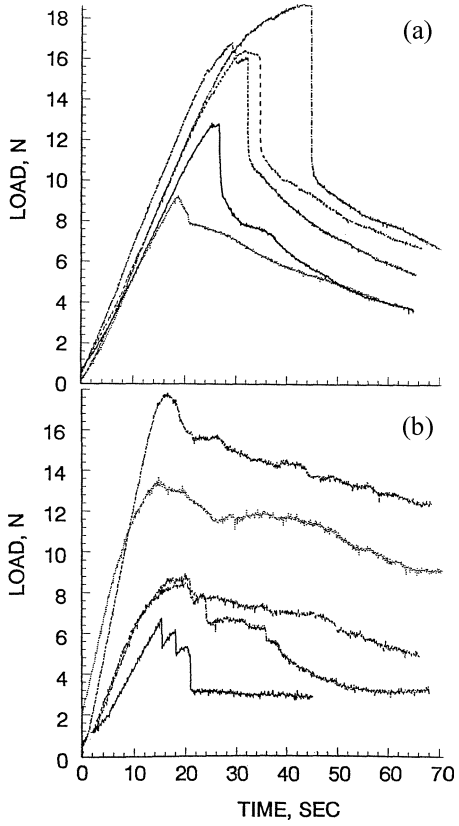


**Figure 9.** Typical load–time profiles of the fiber push-out test on (a) DS sapphire–NiAl and (b) DS sapphire–NiAl(Yb) specimens (note the frictional load undulations during sliding of debonded fibers in the DS NiAl(Yb) material), (c) through (g) are frequency histograms for (c) and (d) proportional shear stress, $\tau_p$, (e) and (f) maximum shear stress, $\tau_m$, and (g) frictional shear stress, $\tau_f$ (data are shown separately for thick ($t > 350$ $\mu$m) and thin ($t < 350$ $\mu$m) discs, except for the $\tau_f$ which was independent of thickness), and (h) fiber push-out data on NiAl- and NiAl(Yb) matrix composites plotted as stress drop ($\tau_m - \tau_f$) versus the maximum shear stress, $\tau_m$.

nucleation of cracks and correspondingly lowest $\tau_p$ values. On the other hand, GI fibers had no coincident grain boundaries to assist crack nucleation and decohesion.

The fiber push-out behavior is influenced by the disk thickness; thin disks bend prior to debond initiation. When the pseudoelastic displacements are plotted (Fig. 8d) as a function of disk thickness at a constant load (which corresponds to the lowest measured proportional shear load of 1.37 N), a pronounced disk thickness dependence and a large dispersion in the data are seen for the fibers in the powder cloth (PC) specimens at small ($t < 350$ $\mu$m) disk thicknesses. On the other hand, the fibers residing within the interior of the NiAl grains in the DS specimens (GI fibers) do not show any measurable disk thickness dependence over the range of thicknesses examined in the study. The interfacial debonding of fibers in the PC specimens (PC fibers), and of fibers anchored at grain boundaries in the

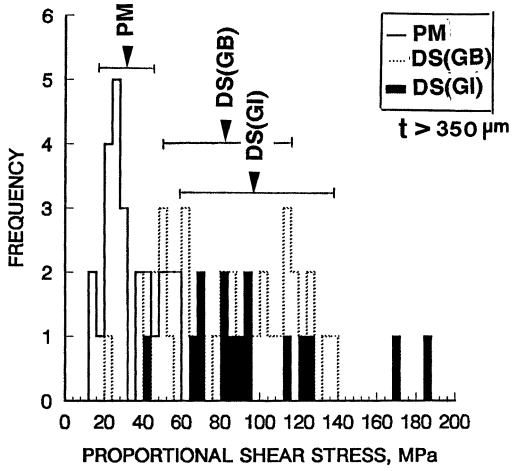


(c)

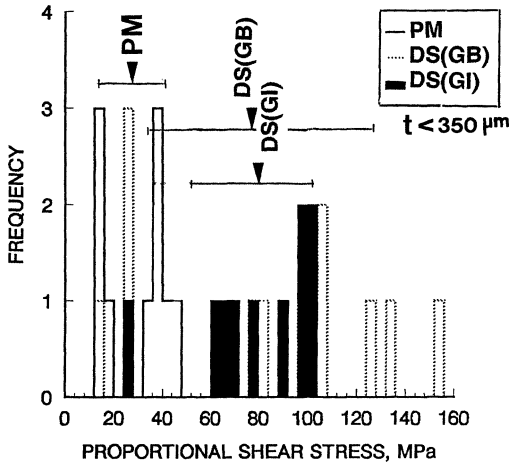


(d)

**Figure 9.** (Continued).

DS specimens (GB fibers) is assisted by the cracking of the matrix grain boundaries coincident on the fibers (Fig. 8b). On the other hand, the fibers within the grain interior (GI fibers) debond without any front-face cracking (Fig. 8c), although fine interfacial cracks form in the matrix on the backfaces where the bending of the disk induces tensile stresses. In the DS specimens, interfacial porosity is seen in the region of displaced fibers (Fig. 8b and c); this porosity formed possibly due to reactions between the binder residues of the PC feedstock that was used for the zone directional solidification. The directional solidification (DS) of samples made from a cast rather than a powder cloth (PC) feedstock [13] did not show such interfacial microvoids and led to higher $\tau_p$ values ($142 \pm 37$ MPa). The NiAl matrix in the region of displaced fibers shows evidence of microplastic grooving by fiber asperities.

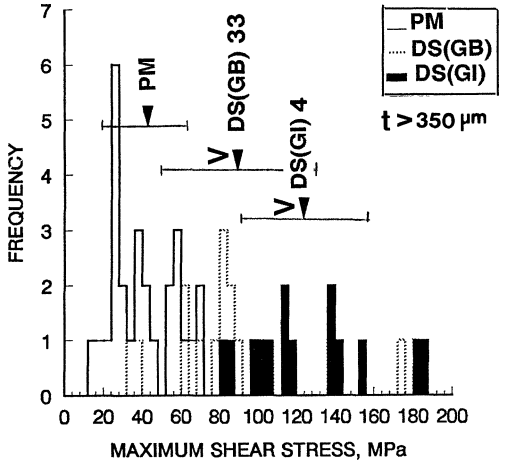


(e)

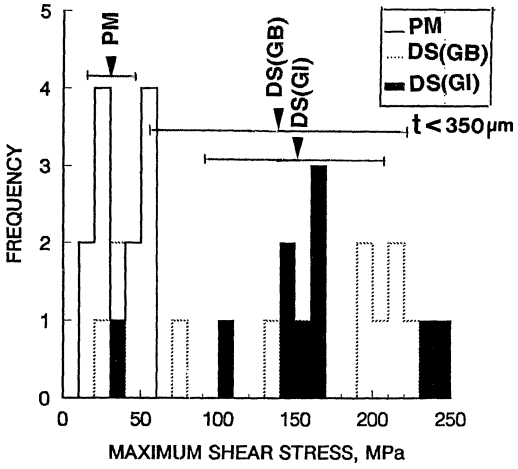


(f)

**Figure 9.** (Continued).

Whereas front- or back face cracks at $\tau_p$ were not detected during the fiber push-out test, a strong acoustic emission (AE) signal was generally observed in the vicinity of the proportional shear stress, $\tau_p$. On the other hand, fiber push-out tests interrupted at $\tau_m$ showed that the test specimens had extensive interfacial front- and back face cracking around those fibers that were anchored at grain boundaries in the PC and DS specimens (the fibers pinned at grain boundaries also showed frequent circumferential decohesion on back faces). On the other hand, fibers that resided within the NiAl grains (GI fibers) did not show front-face interfacial damage, but partial debonding and fine radial cracks were observed on the back faces at $\tau_m$ (Fig. 10a). There were also instances where the fiber fracture preceded debond initiation and propagation as shown in the photomicrographs of Fig. 10b and c.

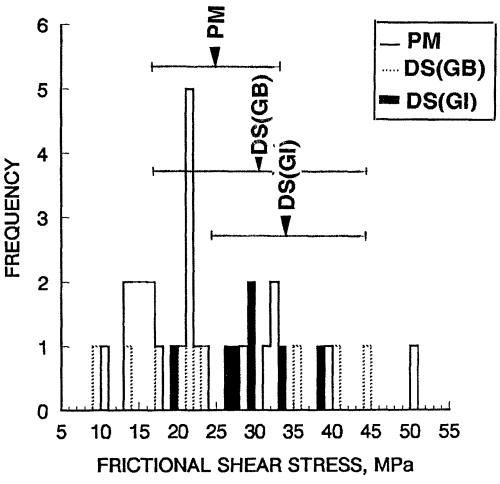


(g)

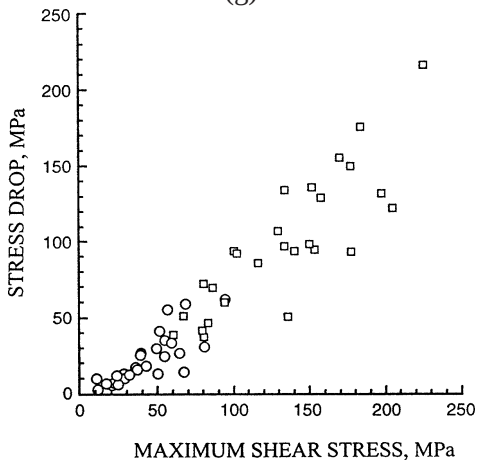


(h)

**Figure 9.** (Continued).

The as-cast (AC) specimens, the DS specimens, and the DS specimens that were subsequently thermal cycled (termed the DS + TC specimens) exhibited higher interfacial strengths than the powder cloth (PC) composites containing the organic binders as seen in Table 1. The thermal cycling (TC) consisted of 500 cycles in air in the temperature range 400 K to 1273 K. As matrix- and fiber fracture was not observed after thermal cycling, the residual stresses were presumably accomodated by matrix plasticity (these stresses could be as high as 900 MPa [13], significantly greater than the yield strength of the matrix, 380 MPa). In the directional solidified (DS) specimens, and in the DS specimens that were thermal cycled (DS + TC specimens), catastrophic debonding occurred in contrast to the as cast (AC) specimens which showed muiltiple step drops in the debond stress due possibly to incremental failure at grain boundaries coincident on the fiber surface.

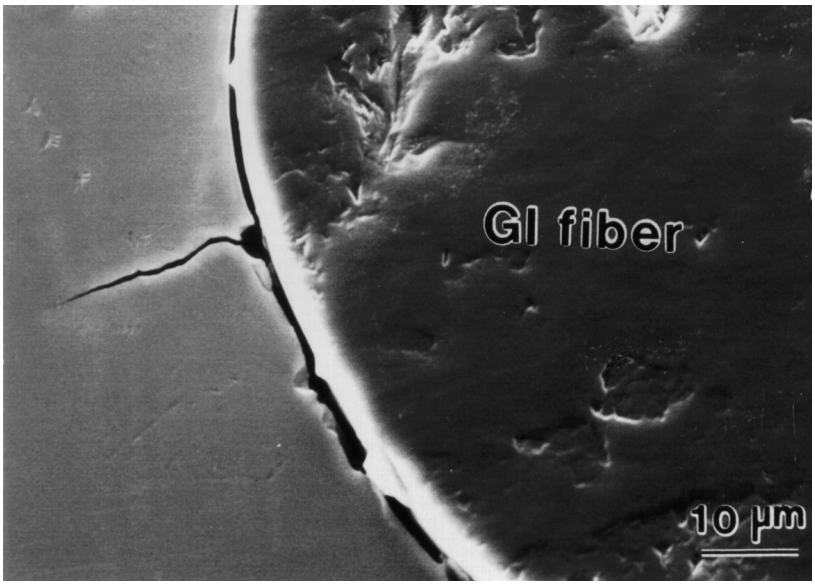


(a)

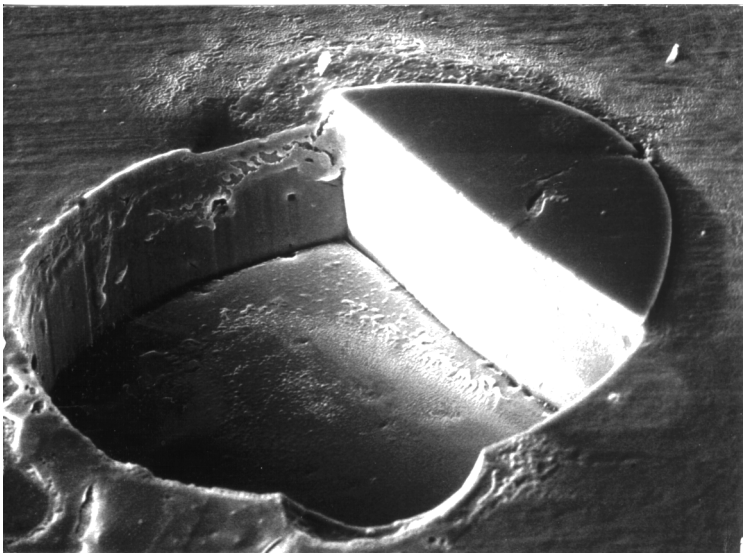

(b)

**Figure 10.** (a) Interfacial decohesion and radial cracking at the maximum shear stress $\tau_m$ on the backface of a GI-fiber in the DS sapphire–NiAl test specimen, (b) and (c) fiber fracture prior to debond initiation and sliding in the DS specimen, (d) front face view- and (e) back face view of debonded interface in a DS NiAl(Yb) test specimen, (f) debonded interface in DS NiAl(Cr) specimen showing Cr precipitation and microplastic grooving of the matrix by fiber asperities, (g) front-face view of a debonded fiber in a DS NiAl(Cr) matrix showing interfacial cracking through intercellular eutectic, (h) back-face view- and (i) front-face view of a debonded fiber in a DS–NiAl(W) test specimen.

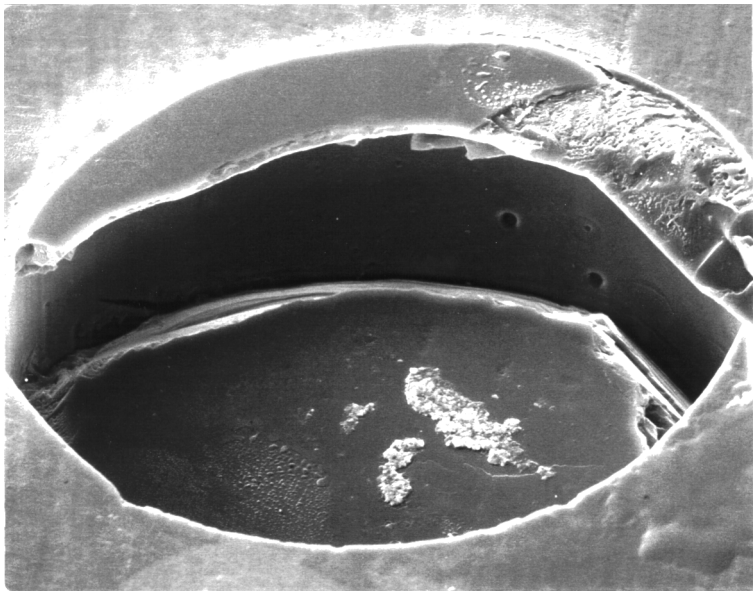

(c)

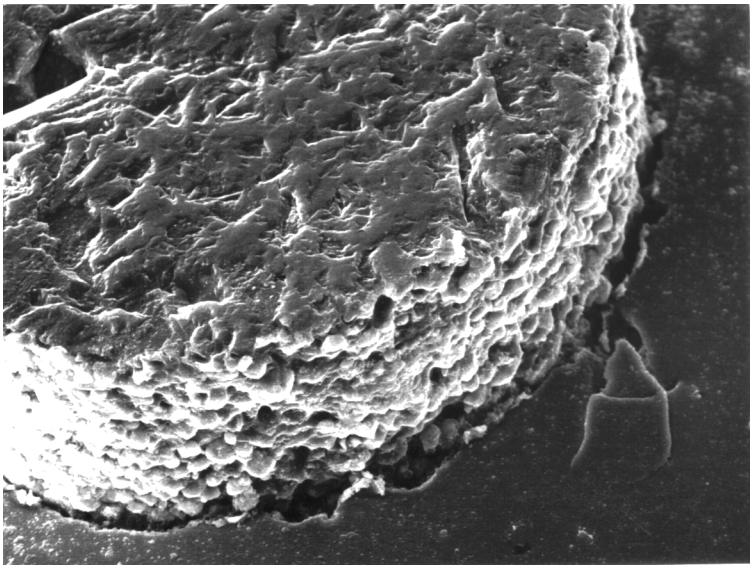

(d)

**Figure 10.** (Continued).

The thermal and mechanical stresses are not uniform over the embedded fiber length and are sensitive to test configuration (e.g. to $t/h$ ratio, where $t$ = disk thickness and $h$ = support span).

The frictional shear stress values for fibers in the powder cloth (PC) specimens, and for the GB fibers and GI fibers in the DS specimens in thin ($<$300 $\mu$m) disks

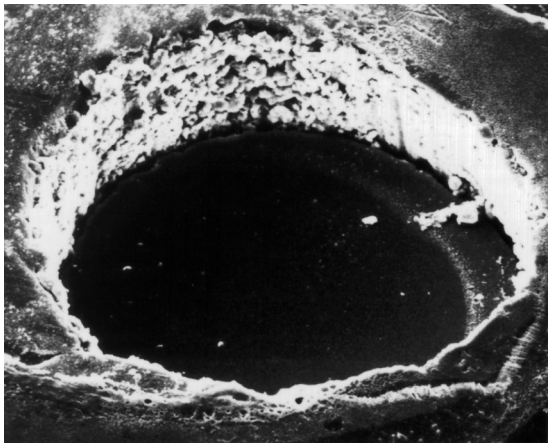

(e)

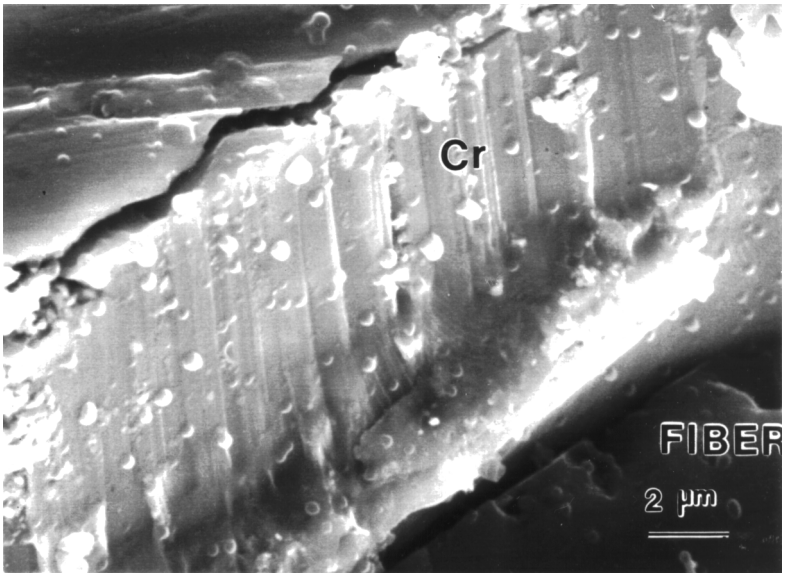


(f)

**Figure 10.** (Continued).



were 20 ± 13 MPa, 42 ± 23 MPa, and 19 ± 9 MPa, respectively. Similarly, the average $\tau_f$ values for fibers in the PC specimens, and for the GB- and GI fibers in thick (>300 $\mu$m) disks were 22 ± 9 MPa, 28 ± 15 MPa, and 32 ± 11, respectively. The relative independence of frictional stress to microstructure surrounding the fibers (i.e. whether the fiber is within the grain or anchored to grain boundaries) suggests that once the fibers are debonded from the matrix, processing history and matrix structure do not affect the stress required for sliding.

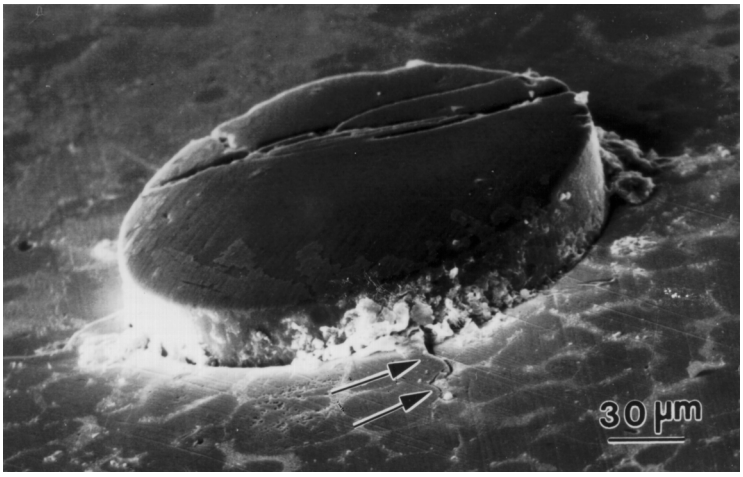


(g)

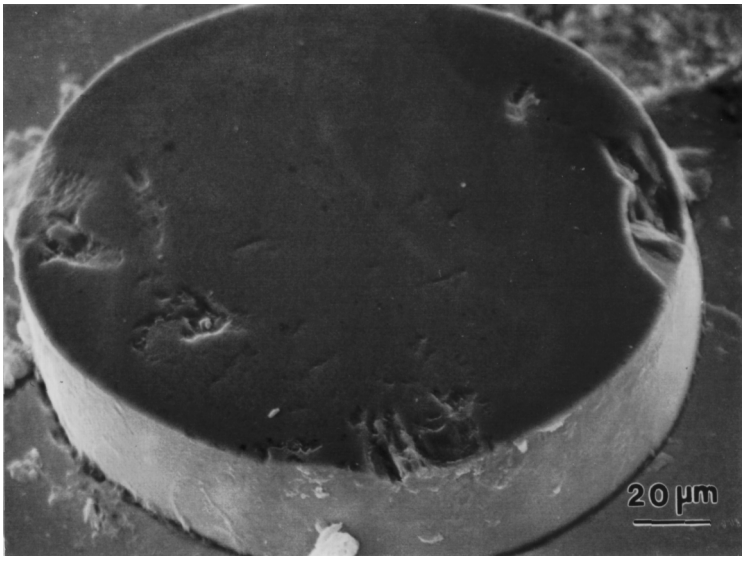


(h)

**Figure 10.** (Continued).

*3.2.2. Sapphire–NiAl(Yb) composites.* In these composites, the stress drop during fiber push-out was gradual rather than abrupt beyond the maximum load; also, large scale fiber sliding exhibited pronounced stress undulations in the frictional regime (Fig. 9b). These undulations are due to the extensive fiber surface reconstruction from chemical attack of the sapphire by the rare earth element ytterbium (Fig. 9d and e). In contrast, the NiAl-matrix composites showed relatively small stress undulations (Fig. 9a). A gradual stress drop has been reported also in the reactive sapphire–Ti–48Al–2Cr–2Nb system where chemical attack of the fiber led to extensive surface roughening. The debond stresses are higher in the

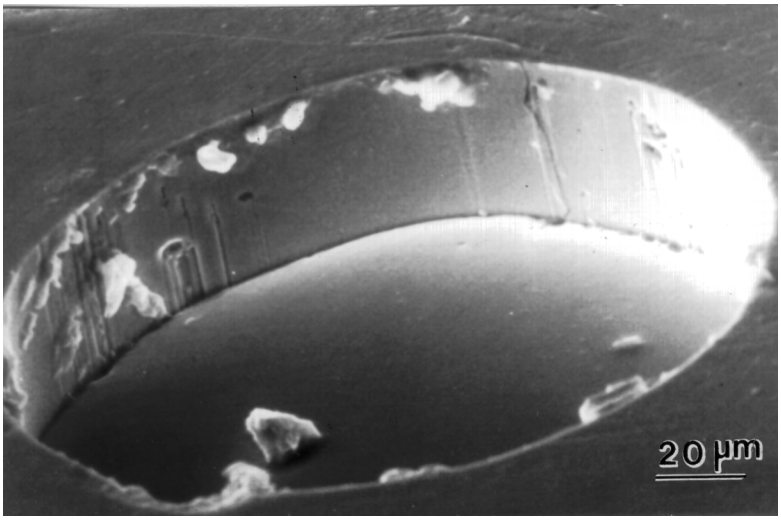


(i)

**Figure 10.** (Continued).

PC- than in the DS NiAl(Yb)-matrix composites in contrast to the behavior of PC and DS sapphire–NiAl composites without ytterbium alloying (the average $\tau_m$ values for PC and DS NiAl(Yb) specimens are 205 ± 69 MPa and 67 ± 44 MPa, respectively, compared to 30 ± 16 MPa and 138 ± 62 MPa for the unalloyed PC and DS composites). Matrix and interfacial cracking, and shrinkage porosities in the DS composites decreased the interfacial shear strength in comparison to the PC sapphire–NiAl(Yb) composites. The frictional stress of PC and DS NiAl(Yb) specimens is larger than that of unalloyed NiAl-matrix composites, and the frictional stress (126 ± 16 MPa) of PC specimens is larger than that of the DS specimens (53 ± 41 MPa). The fiber- and matrix interfaces in the regions of displaced fibers (Fig. 10d and e) show evidence of extensive fiber roughening from chemical attack.

Fiber sliding occurs by geometrical decorrelations of the fiber and matrix asperities at the mating interface; this results in a radial clamping pressure that varies with the sliding distance and with the wavelength and amplitude of the asperity mismatch at the interface. The modulation of the sliding stress due to interfacial roughness has been modeled theoretically in studies that considered growth-related surface flaws in the virgin fiber. However, the growth-related surface flaws on fibers are expected to be geometrically more ordered than the flaws resulting from chemical attack of the fiber surface. As a result, the theoretical calculations of the sliding stress in the latter case is far more difficult. In any case, it must be noted that in brittle-matrix composites, the roughness-induced interfacial shear stress, especially the radial stress, will influence the interface debonding behavior as also the frictional sliding stress of the fibers and the fiber pull-out length.

The shear stresses $\tau_p$, $\tau_m$ and $\tau_f$ were measured over a fairly wide range of $(t/h)$ ratios ($t/h = 0.5$ to 1.8). Figure 9h plots the stress drop at the maximum load $(\tau_m - \tau_f)$ versus $\tau_m$ for the NiAl and NiAl(Yb) composites (see Fig. 8a). Each data point on plots of Fig. 9h represents a test on a separate fiber in a given specimen, or on a fiber from a different test specimen of identical material. This figure shows that the stress drop $(\tau_m - \tau_f)$ increases roughly linearly with $\tau_m$ for $(t/h)$ varying from 0.50 to 1.80; the frictional shear stress, $\tau_f$, is therefore independent of the embedded length of the fiber.



*3.2.3. Sapphire–NiAl(Cr) composites.* The proportional shear stress, $\tau_p$, of as-cast (AC) and directional solidified (DS) NiAl(Cr) composite specimens is higher than that of the as-cast (91 ± 60 MPa) and DS NiAl without Cr (78 ± 32 MPa) (Table 2). After thermal cycling, the $\tau_p$ for both DS NiAl and DS NiAl(Cr) were similar (146 ± 40 MPa for NiAl(Cr) and 142 ± 37 MPa for NiAl), respectively. The mean values of the maximum shear stress, $\tau_m$ (at which complete debonding takes place) for the cast and DS NiAl(Cr) specimens are $>$ 154 ± 55 MPa and $>$ 155 ± 41 MPa compared to the values of 133 ± 79 MPa and 62 to >182 MPa for the cast and DS NiAl specimens without Cr, respectively. After 500 thermal cycles in the temperature range of 400 K to 1273 K, the mean value of the maximum shear strength, $\tau_m$, for AC NiAl(Cr) (considering only the fibers that could be pushed within the loading limit of the machine) decreased from 154 ± 55 MPa to 104 ± 38 MPa whereas it increased from 155 ± 41 MPa to 174 ± 40 MPa in the case of DS specimens. In contrast, the mean $\tau_m$ for NiAl–sapphire was approximately the same before and after thermal cycling (TC).

The mean frictional shear stress values, $\tau_f$, for the as-cast (AC) NiAl(Cr) specimens and cast NiAl(Cr) specimens that were subsequently thermal cycled (AC + TC) are 72 ± 39 MPa and 43 ± 27 MPa respectively, whereas the mean values of $\tau_f$ for the DS and the (DS + TC) specimens are 72 ± 35 MPa and 91 ± 41 MPa, respectively. These values for the NiAl(Cr)-matrix composites are higher than the frictional shear stress values of the as-cast (AC) NiAl specimens, cast and directional solidified (AC + DS) NiAl specimens, powder cloth (PC) NiAl specimens, and directional solidified powder cloth feedstock (PC + DS) NiAl specimens. However, these friction stress values are lower than $\tau_f$ values for the as processed powder cloth (PC) sapphire–NiAl(Yb) composites, and the sapphire–NiAl(Yb) composites that were heat-treated (HT) in the solid-state below the alloy liquidus. In the sapphire–NiAl(Cr) specimens, the chromium precipitates decorate the debonded interfaces and cause matrix grooving during fiber sliding (Fig. 10f); the wear tracks due to fiber sliding are about the same size as Cr precipitates (in contrast, the debonded surfaces were clean and devoid of second phase precipitates in unalloyed NiAl specimens, consistent with the lower frictional stress of these materials). In the sapphire–NiAl(Cr) composites, the fracture path in the composite during fiber push out is predominantly through the intercellular eutectic (Fig. 10g).

The mismatch of the coefficients of thermal expansion (CTE, $\alpha$) between NiAl and alumina [$\alpha_{\text{sapphire}} = 9.5 \times 10^{-6}$ K$^{-1}$ and $\alpha_{\text{NiAl}} = 15 \times 10^{-6}$ K$^{-1}$] is large and results in thermal clamping stresses which are compressive on the fiber and tensile in the surrounding matrix. The large compressive radial stresses created by the thermal clamping over the fiber length tend to increase the magnitude of fiber debond stress during the fiber push out. The thermal clamping stresses are expected to be lower in DS NiAl(Cr) than in DS NiAl, since chromium, which forms an interlayer on the fiber surface, has a lower CTE ($\alpha_{\text{Cr}} = 6.2 \times 10^{-6}$ K$^{-1}$) than NiAl ($\alpha_{\text{NiAl}} = 15 \times 10^{-6}$ K$^{-1}$). The CTE mismatch between the NiAl–Cr eutectic interlayer and the sapphire fiber ($\alpha_{\text{sapphire}} = 9.5 \times 10^{-6}$ K$^{-1}$) and the thermal stresses arising from the CTE mismatch, will be lower in the NiAl(Cr) compared to the NiAl. The higher interfacial shear strengths observed in the AC and DS sapphire–NiAl(Cr) compared to the AC and DS sapphire–NiAl are, therefore, not simply due to thermal clamping and possibly represent the true effects of chemical modification of the fiber–matrix interface by alloying. This is consistent with other studies [46, 47] which show that the wetting angle and the 'push-off' strength of solidified sessile-droplets of nickel on sapphire are improved by the addition of Cr to Ni.

Limited thermal cycling of the NiAl and NiAl(Cr) specimens did not appreciably impair the interface strength (the compliant layer of Cr did not lose its effectiveness due to thermal cycling). However, as thermal cycled samples of NiAl and NiAl(Cr) had low fiber volume fractions (<0.5%), they may not reflect the thermal fatigue resistance of real composites having high fiber volume fraction.

*3.2.4. Sapphire–NiAl(W).* These composites exhibited higher proportional shear strength, $\tau_{\text{p}}$, than the unalloyed sapphire–NiAl composites; however, the maximum shear stress, $\tau_{\text{m}}$, of directional solidified (DS) sapphire–NiAl(W) specimens is higher than DS NiAl but lower than $\tau_{\text{m}}$ of both DS NiAl (>182 MPa) and DS NiAl(Cr) (174 $\pm$ 40 MPa). No interfacial excess of tungsten-rich precipitates is observed on the fibers with up to 1.5 wt% W addition to NiAl. The frictional shear stress in the NiAl(W) matrix composites was generally lower than that in the sapphire–NiAl(Cr) and sapphire–NiAl(Yb) composites, and was comparable to the frictional shear stress in the sapphire–NiAl composites without any alloying additions. The debond interfaces in all sapphire–NiAl(W) specimens were generally clean but showed wear tracks resulting from fiber surface asperities (Fig. 10h and i).

### *3.3. Fiber strength*

*3.3.1. Sapphire–hastealloy composites.* The sapphire fibers in this alloy suffered a severe loss of strength. The extracted fibers were very brittle and difficult to handle. The fiber strength data were analyzed using a two-parameter Weibull distribution function [14] of the form: $F(\sigma) = 1 - \exp(\alpha\sigma^{\beta})$, where $F(\sigma)$ is the failure probability of a fiber of strength, $\sigma$, and $\alpha$ and $\beta$ are the scale parameter,

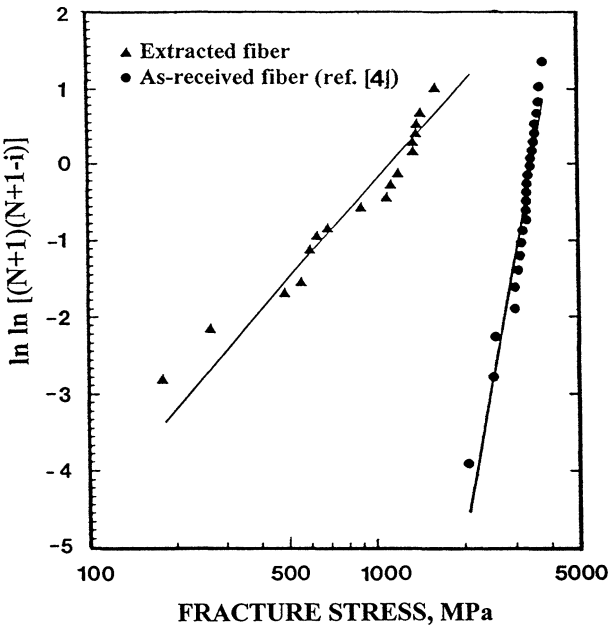


(a)

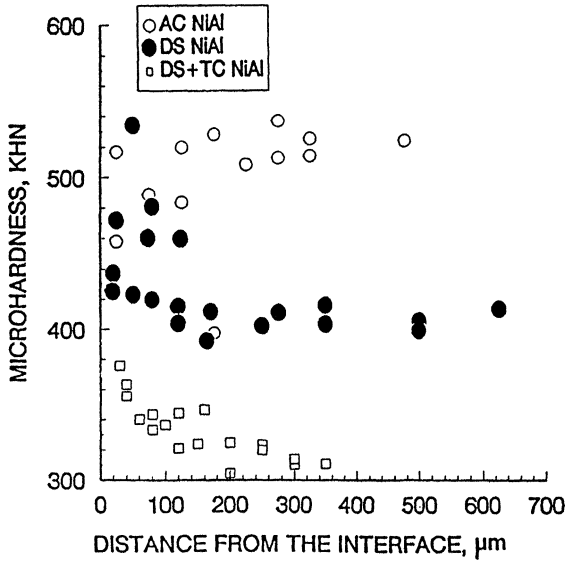


(b)

**Figure 11.** (a) Weibull plots of distribution of room temperature tensile strength of as-received sapphire fibers, and fibers extracted from pressure cast sapphire–hastelloy composites. Mean Weibull strength: 904 MPa, standard deviation: 562 MPa, coefficient of variation: 62 pct, (b) microhardness distribution in the vicinity of fiber–matrix interface in the sapphire–NiAl and sapphire–NiAl(Cr) specimens (AC: as cast, DS: directional solidified, TC: thermal cycled).

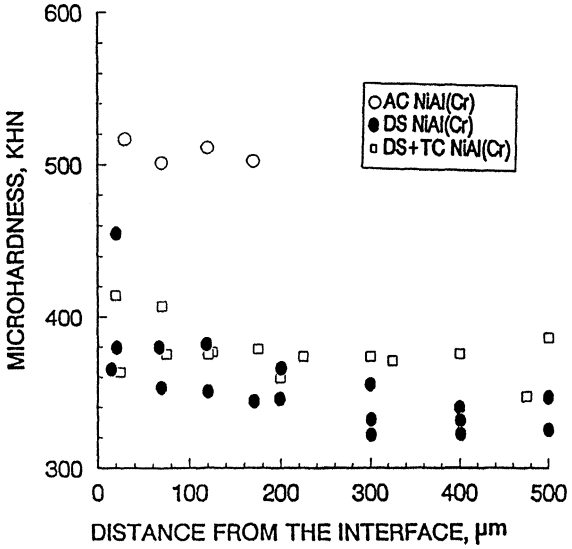


(b)

**Figure 11.** (Continued).

and Weibull modulus, respectively. A Weibull distribution plot of the residual fiber strength data collected in this study is shown in Fig. 11a. The fiber strength will follow a Weibull distribution if a plot of $\ln\ln((N+1)/(N+1-i))$ versus $\ln\sigma$ is linear which is roughly the case in the present situation (Fig. 11a). A least squares fit of the data yielded the equation of straight line as $y = 1.7479x - 12.0997$. The values of the Weibull scale parameter, $\alpha$, and Weibull modulus, $\beta$, are $5.561 \times 10^{-8}$ and 1.7479, respectively. The Weibull mean strength, $\sigma$, standard deviation, $s$, and the coefficient of variation, *CV*, are 904 MPa, 562 MPa and 62.2%, respectively. There was on an average 65% decrease in the fiber strength after pressure casting; the as-received fiber strength is about 2.7 GPa [11] whereas the strength of extracted fibers (average of seventeen tests) is 0.904 GPa. Extensive chemical attack of polycrystalline as well as single crystal alumina fibers also has been noted in pressure cast and powder-processed Fe- and Ni- base intermetallic-matrix composites [7, 8]. The degradation of strength of single crystal sapphire (SaphikonTM) fibers in 'powder-cloth' processed FeCrAlY, FeCrAl, Cr, FeAl and NiAl matrix composites is in the range of 45% to 60% [5, 6], whereas strength degradation in pressure cast $Ni_3Al-Ti$ matrix composites is reported to be 67% [8]. The distribution of residual strength of extracted fibers in all such composites is roughly consistent with the Weibull statistics. It is noteworthy that the damaged fibers are not likely to yield any strengthening. A judicious selection of matrix alloy chemistry, use of reaction barrier coatings and control of processing conditions (e.g. lower temperatures) will likely promote wetting and interfacial bonding while minimizing the strength loss in the reinforcement from chemical attack.

### *3.4. Microhardness*

The microhardness profiles for the NiAl and NiAl(Cr) specimens are shown in Fig. 11b and c. In the as-cast (AC) state, the hardness values for NiAl(Cr) (501 KHN) and NiAl (513 KHN) are comparable. In the DS state, a hardness gradient is noticed; at about 175 $\mu$m from the interface, the hardness gradient is roughly zero. The bulk hardness is somewhat higher in the DS NiAl (400 KHN) than the DS NiAl(Cr) (333 KHN). The thermal cycling reduces the hardness gradient and the hardness of DS NiAl (from 400 KHN to 300 KHN) but does not affect the hardness of DS NiAl(Cr) specimens (in fact, a slight increase is noted, from 333 KHN to 360 KHN, for the DS NiAl(Cr)).

In summary, this study focussed on the response of the fiber–matrix interface in sapphire-reinforced nickel-base high-temperature composites to processing methodology, selected process and material variables (temperature, composition, grain structure), and test variables (disk thickness in the fiber push-out test). In particular, interface microstructure and chemistry, interface strength, deformation and fracture behaviors during the fiber push-out test, fiber residual strength, and microhardness data were reported for sapphire-reinforced nickel aluminide, and a Ni-base superalloy synthesized using one or more of the following techniques: powder cloth process, vacuum induction melting and chill casting, floating zone directional solidification, and pressure infiltration casting. The results highlight the feasibility of designing the composite microstructure by the solidification techniques in these high-temperature composites, yielding improved interfacial shear strength and toughening potential resulting from microstructure design provided that adequate wettability is achieved without appreciable fiber degradation and strength loss.



## 4. CONCLUSIONS

1. The ‘floating-zone’ directional solidification (DS) of sapphire–NiAl composites creates large columnar grains oriented along the fiber axis, with fibers either embedded within the matrix grains or anchored at one-to-three grain boundaries; the progressive elimination of grain boundaries by DS suggests potential to grow single crystal NiAl matrix reinforced with sapphire fibers for improved strength and toughening. The Powder Cloth (PC) and as-cast specimens show fine equiaxed grain structure with some porosity; the DS of PC feedstock specimens led to appreciable interfacial porosity due to binder residues compared to as-cast (AC) specimens.
2. Alloying NiAl with the rare earth element ytterbium leads to a severe chemical attack and extensive reconstruction of the fiber surface; the extent of attack is greater in directional solidified (DS) composites than in Powder Cloth (PC) composites. The products of reaction are $Yb_2O_3$, $Yb_3Al_5O_{12}$, and O-enriched NiAl matrix. The fiber–matrix interfacial shear strength of the sapphire–NiAl(Yb) composites is considerably greater than the strength of all

other sapphire-reinforced NiAl matrix composites examined in this study. The interfacial roughening due to chemical attack of sapphire by Yb resulted in a very large post-debond sliding stress. However, the high interfacial strength is achieved at the expense of the fiber surface quality.

3. The stress–displacement profiles during fiber push out display three stress transitions characterized by the proportional shear stress ($\tau_p$) near the onset of debond initiation, maximum shear stress ($\tau_m$) at which complete debonding takes place, and frictional shear stress ($\tau_f$) for the sliding of debonded fibers through the matrix. A strong acoustic emission response was usually detected near the stress $\tau_p$. The deformation and fracture behaviors of all composites at these stresses are sensitive to processing methodology, matrix composition, grain structure, and the ratio of the test specimen thickness ($t$)-to-support span width ($h$) during fiber push-out. Thick ($t/h > 0.75$) test specimens exhibit an abrupt stress drop at $\tau_m$, whereas thin ($t/h < 0.75$) specimens exhibit a continuous rather than abrupt drop in stress at $\tau_m$. The pseudoelastic bending of test specimens during the fiber push-out is small at $t/h > 0.75-1.0$, with fibers embedded within the NiAl grains in the directional solidified (DS) composites exhibiting least sensitivity to disk thickness at all ($t/h$) values.
4. The matrix grain boundaries (g.b.) anchored on the fibers serve as crack initiation sites during fiber push out. This is borne out by the fact that only the fibers pinned at grain boundaries in DS specimens, and all the fibers in the powder cloth (PC) specimens exhibited low interfacial shear strengths as well as front- and back-face interfacial cracks at $\tau_p$. On the other hand, all the fibers engulfed within the NiAl grains in the directional solidified (DS) specimens led to significantly higher interface strength and exhibited interfacial decohesion and radial cracks only at specimen back-faces at stresses close to the maximum shear stress, $\tau_m$. The maximum debond stresses were the highest for the fibers engulfed within the grains in the DS (and as cast) specimens, followed by the fibers pinned at grain boundaries in the DS specimens, and the fibers in the powder cloth (PC) composites. This suggests that matrix polycrystallinity influences the measurements of interfacial strengths using the fiber push-out test. The frictional shear stress, $\tau_f$, is largely independent of the processing history, and the grain structure in the vicinity of the fiber, but exhibits a strong dependence on the alloying additions to the matrix.
5. Alloying NiAl with Cr and W increases the interfacial shear strength in sapphire-reinforced NiAl matrix composites in both the as cast (AC) and DS conditions with relatively little additional fiber degradation. Chromium-rich eutectic deposits preferentially at the interface, and forms a dual-phase microstructure suggesting possible room-temperature toughening potential. On the other hand, no tendency for preferred deposition at the interface was noted for tungsten-rich eutectic in the sapphire–NiAl(W) composites, although a significant increase in the interfacial shear strength was noted in comparison to the unalloyed sapphire–NiAl composites. Thermal cycling

only marginally decreased the interface strength in low fiber volume fraction (<0.5%) composites. Additionally, a microhardness gradient existed in the matrix near the fiber–matrix interface due to thermal stresses; the thermal cycling only marginally affected the hardness gradient in the low-fiber volume fraction composites.

6. Infiltration in the top-fill configuration (melt on top, preform at the bottom) of densely packed sapphire fiber preforms by a Ni-base superalloy (hastelloy) led to acceptable composite castings when infiltration was carried out with argon gas at pressures of 3.5 MPa or less, and melt temperatures of 1500 to 1600°C. Sapphire was extensively attacked by the matrix, resulting in a strength loss of about 65% relative to the virgin fibers, in contrast to the reported strength loss of 45 to 60% in solid-state fabricated sapphire-reinforced intermetallic and superalloy composites. The strength distribution of fibers extracted from the pressure cast matrix was consistent with a Weibull distribution function.



*Acknowledgements*

This work was supported by grants from NASA and the U.S. National Academy of Sciences through National Research Council. Thanks are due Mr. T. K. Glasgow, Dr. R. R. Bowman, and Dr. J. I. Eldridge of NASA Lewis Research Center, Cleveland, for support and encouragement. RA would like to express his sincere appreciation to Prof. S. T. Mileiko of the Institute of Solid State Physics, Russian Academy of Sciences, for helpful discussion on interfaces in high-temperature composites, and to Dr. Robert Berkemer, Chair, Technology Department, and Dr. T. K. Knous, Associate Dean for Research, UW-Stout for encouragement.

## REFERENCES

1. R. D. Noebe, R. R. Bowman and J. I. Eldridge, Initial evaluation of continuous fiber-reinforced NiAl composites, in: *MRS Symp. Proc., Vol. 194 (Intermetallic Matrix Composites)*, D. L. Anton, R. McMeeking, D. B. Miracle and P. Martin (Eds), pp. 323–331. Materials Research Society (MRS) (1990).
2. R. A. MacKay, S. L. Draper, A. M. Ritter and P. A. Siemers, A comparison of the mechanical properties and microstructures of intermetallic-matrix composites fabricated by two different methods, *Metall. Mater. Trans.* **25A**, 1443–1455 (1994).
3. N. Stoloff and D. E. Alman, Innovative processing techniques for intermetallic-matrix composites, in: *MRS Symp. Proc., Vol. 194 (Intermetallic Matrix Composites)*, D. L. Anton, R. McMeeking, D. B. Miracle and P. Martin (Eds), pp. 31–43. Materials Research Society (MRS) (1990).
4. S. L. Draper and I. E. Locci, Alumina fiber strength degradation in metal- and intermetallic-matrix composites, *J. Mater. Res.* **9** (6), 1397–1411 (1994).
5. D. P. Miller, J. J. Lannutti, W. O. Soboyejo and R. D. Noebe, Properties of functionally graded NiAl/alumina composites, in: *Structural Intermetallics*, R. Darolia, J. J. Lewandowski, C. T. Liu, P. L. Martin, D. B. Miracle and M. V. Nathal (Eds), pp. 783–790. The Minerals, Metals and Materials Society (TMS) (1993).
6. W. Hu, W. Wunderlich and G. Gottstein, Interfacial chemical stability during diffusion bonding of alumina fibers with $Ni_3Al$ and NiAl matrices, *Acta Mater.* **44** (6), 2383–2396 (1996).

7. J. Sorensen, Intermetallic-matrix composites, in: *Structural Intermetallics*, R. Darolia, J. J. Lewandowski, C. T. Liu, P. L. Martin, D. B. Miracle and M. V. Nathal (Eds), pp. 717–723. The Minerals, Metals and Materials Society (TMS) (1993).
8. C. G. McKamey, G. L. Povirk, J. A. Horton, T. N. Tiegs and E. K. Ohriner, Fabrication and mechanical properties of $Ni_3Al$-$Al_2O_3$ composites, in: *MRS Symp. Proc., Vol. 194 (Intermetallic Matrix Composites)*, D. L. Anton, R. McMeeking, D. B. Miracle and P. Martin (Eds), pp. 609–614. Materials Research Society (MRS) (1990).
9. S. Nourbakhsh, O. Sahin, W. H. Rhee and H. Margolin, Pressure casting of a Zirconia-toughened alumina fiber-reinforced NiAl composite, *Metall. Trans.* **22A**, 3059–3064 (1991).
10. S. Nourbakhsh, H. Margolin and F. H. Liang, Microstructural of a pressure cast $Fe_3Al$ intermetallic alloy composite reinforced with zirconia-toughened alumina fibers, *Metall. Trans.* **21A**, 2881–2889 (1990).
11. D. M. Shah, D. L. Anton and C. W. Musson, Feasibility study of intermetallic composites, in: *MRS Symp. Proc., Vol. 194 (Intermetallic Matrix Composites)*, D. L. Anton, R. McMeeking, D. B. Miracle and P. Martin (Eds), pp. 333–340. Materials Research Society (MRS) (1990).
12. R. Asthana, S. N. Tewari and S. L. Draper, Strength degradation of sapphire fibers during pressure casting of a sapphire-reinforced Ni-base superalloy, *Metall. Mater. Trans.* **29A**, 1527–1530 (1998).
13. S. N. Tewari, R. Asthana and R. D. Noebe, Interfacial shear strength of cast and directionally solidified NiAl-sapphire fiber composites, *Metall. Trans.* **24A**, 2119–2125 (1993).
14. S. N. Tewari, R. Asthana, R. Tiwari and R. Bowman, Influence of interfacial reactions on the fiber push-out behavior in a sapphire-reinforced NiAl(Yb) composite, in: *Control of Interfaces in Composites*, R. Y. Lin and S. G. Fishman (Eds), pp. 255–273. The Minerals, Metals and Materials Society (TMS) (1994).
15. R. Asthana, S. N. Tewari and R. R. Bowman, Influence of fabrication technique on the fiber push-out behavior in a sapphire-reinforced NiAl matrix composite, *Metall. Mater. Trans.* **26A**, 209–223 (1995).
16. S. N. Tewari, R. Asthana, R. Tiwari, R. Bowman and J. Smith, Influence of interfacial reactions on the fiber–matrix interfacial shear strength in sapphire fiber-reinforced NiAl(Yb) composites, *Metall. Trans.* **26A**, 477–491 (1995).
17. R. Asthana, R. Tiwari and S. N. Tewari, Influence of Cr and W alloying on the fiber–matrix interfacial shear strength in cast and directionally solidified sapphire–NiAl composites, *Metall. Mater. Trans.* **26A**, 2175–2184 (1995).
18. R. Asthana, S. N. Tewari and R. R. Bowman, Influence of fabrication technique and alloying on the interfacial shear strength of sapphire-reinforced NiAl matrix composites, in: *High Performance Composites — Commonalty of Phenomena*, K. K. Chawla, P. K. Liaw and S. G. Fishman (Eds), pp. 21–33. The Minerals, Metals and Materials Society (TMS) (1994).
19. S. N. Tewari, R. Asthana and R. D. Noebe, Fiber push-out behavior in cast and directionally solidified sapphire–NiAl composites, in: *Proc. of First International Conference on Processing Materials for Properties (PMP '93)*, H. Henein and T. Oki (Eds), pp. 995–998. The Minerals, Metals and Materials Society (TMS) (1993).
20. S. N. Tewari, R. Asthana, R. Tiwari and R. Bowman, Zone directional solidification of sapphire–NiAl composites, *NASA HITEMP REVIEW-1993*, NASA Conf. Publ. 19117, Vol. 2, Compressor/Turbine Materials, 60.1–60.11, NASA.
21. K. K. Chawla, *Composite Materials-Science and Engineering*. Springer-Verlag, (1987).
22. S. Nourbakhsh, O. Sahin, W. H. Rhee and H. Margolin, Microstructure of alumina fiber-reinforced superalloy (INCONEL 718) composites, *Metall. Mater. Trans.* **27A**, 451–458 (1996).
23. X. F. Chen, D. R. Johnson and B. F. Oliver, Microstructures from a directionally solidified NiAl-Cr eutectic deformed at room temperature, *Scripta Metall. Mater.* **30** (8), 975–980 (1994).
24. T. Hirano and T. Mawari, Unidirectional solidification of $Ni_3Al$ by a floating zone method, *Acta Metall. Mater.* **41** (6), 1783–1789 (1993).

25. R. Darolia, NiAl alloys for high-temperature structural applications, *J. Metals* **43** (3), 44–48 (1991).
26. R. D. Noebe, A. Misra and R. Gibala, Plastic flow and fracture of B2 NiAl-based intermetallic alloys containing a ductile second phase, *J. Iron Steel Inst. Jpn.* **31** (10), 1172–1185 (1991).
27. J. I. Eldridge, Desktop Fiber Push-Out Apparatus, *NASA TM 105341*, National Aeronautics and Space Administration, (Dec. 1991).
28. S. Ochiai and K. Osamura, *Metall. Trans.* **19A**, 1499 (1998).
29. Sapphire and Advanced Single Crystal Technologies (Data Sheet), Saphikon Inc., Milford, NH.
30. J. I. Eldridge and B. T. Ebihara, Fiber push-out testing apparatus for elevated temperatures, *J. Mater. Res.* **9** (4), 1035–1042 (1994).
31. M. N. Kallas, D. A. Koss, H. T. Hahn and J. R. Hellman, Interfacial stress state present in a thin-slice fiber push-out test, *J. Mater. Sci.* **27** (14), 3821–3826 (1992).
32. T. J. Mackin, P. D. Warren and A. G. Evans, Effects of fiber roughness on interface sliding in composites, *Acta Metall. Mater.* **40** (6), 1251–1257 (1992).
33. T. J. Mackin, J. Yang and P. D. Warren, Influence of fiber roughness on the sliding behavior sapphire fibers in TiAl and glass matrices, *J. Amer. Ceram. Soc.* **75** (12), 3358–3362 (1992).
34. P. D. Jero, R. J. Kerans and T. A. Parthasarthy, Effect of interfacial roughness on the frictional stresses measured using push-out tests, *J. Amer. Ceram. Soc.* **74** (110), 2793–2797 (1991).
35. C. A. Moose, D.A. Koss and J. R. Hellman, Interfacial shear behavior of sapphire-reinforced NiAl composites, in: *MRS Symp. Proc., Vol. 194 (Intermetallic Matrix Composites)*, D. L. Anton, R. McMeeking, D. B. Miracle and P. Martin (Eds), pp. 293–299. Materials Research Society (MRS) (1990).
36. J. I. Eldridge and P. K. Brindley, Investigation of interfacial shear strength in a SiC fiber/Ti-24Al-11Nb composite by a fiber push-out technique, *J. Mater. Sci. Lett.* **8**, 1451–1454 (1989).
37. D. B. Marshall, An indentation method for measuring matrix/fiber frictional stresses in ceramic composites, *J. Amer. Ceram. Soc.* **67** (12), c259–c260 (1984).
38. E. P. Rhyne, J. R. Hellman, J. M. Galbraith and D. A. Koss, Thin-slice fiber push-out and specimen bending in metallic-matrix composite test, *Scripta Metall. Mater.* **32** (4), 547–552 (1995).
39. T. A. Parthasarthy, P. D. Jero and R. J. Kerans, Extraction of interface properties from a fiber push-out test, *Scripta Metall. Mater.* **25**, 2457–2462 (1991).
40. T. A. Parthasarthy, D. R. Barlage, P. D. Jero and R. J. Kerans, Effect of interfacial roughness parameters on the fiber push-out behavior of a model composite, *J. Amer. Ceram. Soc.* **77** (12), 3232–3236 (1994).
41. W. C. Carter, E. P. Butler and F. R. Fuller, Jr., Micro-mechanical aspects of asperity-controlled friction in fiber-toughened ceramic composites, *Scripta Metall. Mater.* **25**, 579–584 (1991).
42. D. B. Marshall, M. C. Shaw and W. L. Morris, Measurement of interfacial debonding and sliding resistance in fiber-reinforced intemetallics, *Acta Metall. Mater.* **40** (3), 443–454 (1992).
43. R. J. Kerans, P. D. Jero, T. A. Parthasarthy and A. Chatterjee, Determination of fiber/matrix interface mechanical properties in brittle-matrix composites, in: *MRS Symp. Proc., Vol. 194 (Intermetallic Matrix Composites)*, D. L. Anton, R. McMeeking, D. B. Miracle and P. Martin (Eds), pp. 263–270. Materials Research Society (MRS) (1990).
44. R. Asthana and S. N. Tewari, Processing effects on the interfacial sliding of debonded fibers in a sapphire–NiAl(Yb) composite, *J. Mater. Sci. Lett.* **16**, 406–411 (1997).
45. M. D. Thouless, Frictional sliding and pull-out of a fiber, *Scripta Metall. Mater.* **27**, 1211–1214 (1992).
46. P. Kritsalis, V. Merlin, L. Coudurier and N. Eustathopoulos, Effect of Cr on interfacial reaction and wetting mechanisms in Ni alloy/alumina systems, *Acta Metall. Mater* **40** (6), 1167–1175 (1992).
47. R. M. Crispin and M. Nicholas, The wetting and bonding behavior of some nickel alloy-alumina systems, *J. Mater. Sci.* **11**, 17–21 (1976).